Implementation of a Calibration Algorithm for Efficient Modeling of Direction-Dependent and Baseline-Dependent Effects for Interferometric Imaging Arrays in Radio Astronomy

by

Anathi Hokwana

Thesis presented in partial fulfilment of the requirements for the degree of Master of Engineering (Electronic) in the Faculty of Engineering at Stellenbosch University

Department of Electrical and Electronic Engineering,
University of Stellenbosch,
Private Bag X1, Matieland 7602, South Africa.

Supervisor:

Prof. D.B. Davidson

March 2017

Stellenbosch University https://scholar.sun.ac.za

Declaration

By submitting this thesis electronically, I declare that the entirety of the work contained therein is my own, original work, that I am the sole author thereof (save to the extent explicitly otherwise stated), that reproduction and publication thereof by Stellenbosch University will not infringe any third party rights and that I have not previously in its entirety or in part submitted it for obtaining any qualification.

Date: March 2017 .....

Copyright © 2017 Stellenbosch University
All rights reserved.

Stellenbosch University https://scholar.sun.ac.za

Abstract

Implementation of a Calibration Algorithm for Efficient Modeling of Direction-Dependent and Baseline-Dependent Effects for Interferometric Imaging Arrays in Radio Astronomy

A. Hokwana

Department of Electrical and Electronic Engineering,
University of Stellenbosch,
Private Bag X1, Matieland 7602, South Africa.

Thesis: MEng (Electronic)

December 2016

This thesis presents the implementation of the *Högbom* Clean and the A-Stacking algorithms. Radio interferometric imaging arrays are subject to various direction-dependent effects, such as manufacturing tolerances of the antennas, mutual coupling and ionospheric delays. Since these direction-dependent effects are different for every baseline, the Fourier relationship between the intensity function and the visibility function breaks down, as the measured visibilities are no longer related to the same apparent sky.

This break down in the Fourier relationship implies that the efficiency of the Fast Fourier Transform (FFT) in computing the backward calculation (visibility to sky) can no longer be employed due to the effects introduced in the gain matrix. A linear model called A-Stacking is used to correct for these effects and provides a trade-off between accuracy and computational efficiency. In this work, FEKO simulations for LOFAR-like and PAPER-like interferometer arrays have been computed with special interests in direction-dependent effects due to mutual coupling of these arrays.

The efficiency of the *Högbom* Clean algorithm have been investigated and as expected, found to perform better for point source-like structure than extended structure. The perfomance of the A-Stacking algorithm has also been investigated, and a simple trade off between accuracy and computational cost when computing the forward calculation (sky to visibility) is shown.

Stellenbosch University https://scholar.sun.ac.za

Uittreksel

Implementasie van ‘n Kalibrasie Algoritme vir die Effektiewe modellering van direksie en basislyn afhanklike effekte vir Interferometriese Beelding Skikkings in Radio Astronomie

A. Hokwana

Departement Elektriese en Electroniese Ingenieurswese,
Universiteit van Stellenbosch,
Privaatsak X1, Matieland 7602, Suid Afrika.

Tesis: MIng (Elektroniese)

Desember 2016

In hierdie werkstuk word die implementasie van die “*Högbom* Clean” en die “A-Stacking” algoritmes verduidelik. Radio interferometriese beelding samestellings word beïnvloed deur verskeie nigting afhanklike effekte, soos vervaardigingstoleransie van die antennas, wedersydse koppeling en ionosferiese vertragings. Bogenoemde effekte is anders vir elke basislyn en veroorsaak dat die Fourier transformasie tussen die intensiteit en sigbaarheid funksies afbreek. Die rede hiervoor is dat die gemete sigbaarheid nie meer verwant is aan die dieselfde oënskynlike ruimte nie.

Die afbreek van die Fourier transformasie verhouding impliseer dat die effektiwiteit van die Vinnige Fourier Transformasie (VFT) nie meer van toepassing is nie, hoofsaaklik weens effekte wat in die aanwins matriks voorgestel word. ‘n Lineêre model, genaamd die “A-Stacking” algoritme word gebruik om hierdie effekte te korrigeer. In hierdie navorsing word FEKO simulasies van die LOFAR en PAPER tipe antenna samestellings gebruik om nigting afhanklike effekte, voorgestel weens wedersydse koppeling, te analiseer.

Die effektiwiteit van die “ *Högbom* Clean” algoritme word ook ondersoek en daar word gevind dat dit beter werk vir puntbron tipe, eerder as uitgebreide strukture. Die gedrag van die “A-Stacking” algoritme beeld ook ‘n goeie balans tussen akkuraatheid en berekenings-koste (in terme van rekenaargeheue en looptyd) uit, spesifiek tydens die berekening van voorwaartse stap (beeld tot sigbaarheid).

Stellenbosch University https://scholar.sun.ac.za

Acknowledgements

I am very grateful for my academic career and to all distinguished academics who have played a pivotal role in my development as a human being and as a student. This journey has been massively fruitful both academically and personally. It would be indecorus of me not to acknowledge the following people and institutions whose support i am extremely grateful for.

Above all, i would be remiss not to acknowledge one man; my supervisor. I wish to extend my sincerest gratitude to Prof D.B Davidson; for his patiance, understanding and guidance throughout my stay at Stellenbosch University. Not even once has he ever made me feel inferior in any way and has always given me the time to wonder and find solutions. I have come to learn and grow so much under his supervision, not just academically but personally too and for that i am grateful. I would like to express my sincere gratitude to Dr D. Smith for his guidance and support during his time at Stellenbosch University. For all the discussions and general insights, i am extremely grateful. I am indebted to Dr A. Young for his guidance and willingness to help even after leaving Stellenbosch. The lengthy email discussions and the Saturday long skype sessions, i am very greatfull for your help. I am grateful to Dr D. Ludick for his help and assistance with FEKO related issues and all the discussions we had, which have contributed immensely to the development of this thesis.

I would also like to thank my colleagues past and present in the penthouse for their informal discussions which have also proved very valuable to the completion of this thesis. A special mention to my brothers, Ngoy and TJ whom were always willing to lend an ear even though they had their own work and deadlines to meet. I am thankful and appreciate everyone who has contributed in one way or another to the completion of this work, including the NASSP administrators at UCT and Alan who has widened my horizon interms of how i viewed academics.

To the University of Stellenbosch and to the SKA, my sincere gratitude for the funding during and throughout the duration of my studies. It would not have been possible without the support and encouragement of my family to even have undertaken this journey, and for that i am extremely grateful. It would be improper of me not to single out my mother whom i probably don't thank enough,

Stellenbosch University https://scholar.sun.ac.za

to express my infinite gratitude for all the invaluable support and encouragement. Finally, with the understanding that none of what i have achieved is due to my intelligence or hard work as an individual, but the grace of the almighty. I thank God for all I have been able to achieve and accomplish.

Stellenbosch University https://scholar.sun.ac.za

Dedications

I dedicate this work to my late grandparents
and
to my mother.

Stellenbosch University https://scholar.sun.ac.za

Contents

Declaration i

Abstract ii

Uittreksel iii

Acknowledgements iv

Dedications vi

Contents vii

List of Figures ix

List of Tables xi

Nomenclature xii

1 Introduction 1
- 1.1 Background . . . 1
- 1.2 Problem Statement . . . 6
- 1.3 The Document Outline . . . 7

2 Antenna elements 8
- 2.1 Introduction . . . 8
- 2.2 Antennas . . . 8
- 2.3 Antenna Properties . . . 9
- 2.4 Dipole Antenna . . . 11
- 2.5 Conclusion . . . 21

3 Radio Interferometers and Aperture Synthesis 23
- 3.1 Introduction . . . 23
- 3.2 The Quest for Angular Resolution, θ. . . . 23
- 3.3 The 2-Element Interferometer Conceptualization . . . 24
- 3.4 Earth Rotation Aperture Synthesis . . . 25
- 3.5 The co-ordinate system and antenna spacings . . . 26

Stellenbosch University https://scholar.sun.ac.za

3.6 The Visibility, Intensity Distribution Function and the uv-Coverage 28
3.7 The Synthesised beam and the weighting functions 32
3.8 Conclusion 36

4 Deconvolution and the CLEAN algorithm 38
4.1 Introduction 38
4.2 Deconvolution 38
4.3 The CLEAN Algorithm 44
4.4 CLEAN Variations 52
4.5 Conclusion 53

5 The A-Stacking Algorithm 54
5.1 Introduction 54
5.2 A-Stacking 54
5.3 The A-Stacking formulation 57
5.4 A-Stacking: Backward calculation 61
5.5 Conclusion 62

6 Results and Conclusions 63
6.1 Introduction 63
6.2 The Simulation Procedure 63
6.3 Conclusion 67

7 Conclusion and Future Works 69
7.1 Conclusion 69
7.2 Future Works 70

Appendices 71

A Radio Interferometry Measurement Equation 72
A.1 The Radio Interferometry Measurement Equation (RIME) 72

List of References 75

Stellenbosch University https://scholar.sun.ac.za

List of Figures

1.1 The electromagnetic Spectrum. Image Credit: *NRAO* 1

2.1 An illustration of a guided wave connection [1]. 8
2.2 An illustration of an unguided wave connection [1]. 9
2.3 A schematic representation of the near and far-field regions [2]. 10
2.4 Randomly generated LOFAR-like antenna array using FEKO with bottom port excited with 75Ω. 12
2.5 Randomly generated PAPER-like antenna array using FEKO, excited at the lower port with 75Ω. 12
2.6 Variations in the reflection coefficient for LOFAR element due to mutual coupling effects. 13
2.7 Variations in antenna reflection of PAPER element due to mutual coupling. 13
2.8 The airial view of the core of LOFAR in Netherlands [3] 14
2.9 The structure of the LOFAR LBA antenna [4]. 15
2.10 The model of the LOFAR-like antenna. 16
2.11 The radiation pattern of the LOFAR-like antenna at the edges of the frequency band. 17
2.12 The Reflection Coefficient of the LOFAR-like antenna, appearing to be best resonant at half-wavelength. 18
2.13 Illustration of the real and imaginary impedences of the LOFAR-like antenna element. computed from FEKO. 18
2.14 A single PAPER antenna from the SKA site in South Africa [5] 20
2.15 The FEKO model of the PAPER-like antenna. 21
2.16 The reflection coefficient of the PAPER-like antenna. 21
2.17 The radiation pattern of the PAPER-like antenna. 22

3.1 Image showing the synthesized aperture from the VLA. Credit: NRAO . 24
3.2 Figure showing a two element interferometer [1] 24
3.3 The antenna positions on the ground for an East-West interferometer. 26
3.4 The uv-tracks for a 90 degrees declination as traced by the projected baseline with time of 6 hours. 26
3.5 The antenna positions on the ground for a SW-NE configuration. . . . 27

Stellenbosch University https://scholar.sun.ac.za

3.6 The uv-tracks for a 90 degrees declination as traced by the projected baseline over a time of 6 hours and antennas positioned in a SW-NE configuration. . . . 27
3.7 The sky and uvw coordinates [6] . . . 28
3.8 This is the adopted coordinate system [7]. . . . 31
3.9 Antenna configuration of a VLA-like interferometer. . . . 32
3.10 The uv-coverage for a 6 hours observation of a source at 45° declination with the VLA-like interferometer. . . . 32
3.11 The uv-coverage at declination 90° for a 6 hour observation. . . . 33
3.12 The uv-coverage for 45° declinations for a 2 hour observation . . . 33
3.13 The uv-coverage of a snapshot at 45° declination . . . 34
3.14 The Tapering weighting function . . . 34
3.15 The Uniform weighting . . . 35
3.16 The Natural weighting . . . 36

4.1 An image of a randomly generated sky $I(l,m)$. . . . 42
4.2 The corresponding computed dirty image $I^{'}(l,m)$. . . . 42
4.3 The PSF using a VLA-like array configuration. . . . 43
4.4 Pseudocode for the *Högbom* Clean algorithm as implemented in this chapter. . . . 45
4.5 The relationship between number of iterations and residual flux during the iterative CLEANing procedure. . . . 46
4.6 Residual image as obtained at the end of the iterative subtraction by CLEAN. . . . 47
4.7 The restored image after the CLEANing procedure. . . . 47
4.8 A random Extended source created using Matlab. . . . 48
4.9 Dirty image of the extended source. . . . 48
4.10 Intensity magnitude vs Number of iterations. . . . 49
4.11 Extended source residual image. . . . 49
4.12 Extended source restored image. . . . 50

5.1 Schematic representation of the A-Stacking algorithm; first part illustrating the use of the FFT + degridding and the second part highlighting the computation using the DFT. . . . 58
5.2 Accuracy of the forward calculation vs number of basis functions . . . 60

6.1 Sky model of the extended source simulated using Matlab. . . . 64
6.2 5 random point sources of varying intensities simulated in Matlab. . . . 64
6.3 LOFAR LBA like random array . . . 65
6.4 Weighted Beams . . . 66
6.5 Flux amplitude decreasing with increasing number of iterations for an extended source structure. . . . 67
6.6 A simple tradeoff between the accuracy and the number of iterations (computational cost) of the A-Stacking algorithm. . . . 68

Stellenbosch University https://scholar.sun.ac.za

List of Tables

1.1 Minimum and maximum baseline between antenna elements [8] [9]. . 4
1.2 Computed FF values for each antenna element [8] [10]. 4
1.3 The required characteristics of the two antenna arrays in order to compute FF values for each antenna element 5

2.1 Table showing the design specifications and characteristics of LOFAR [11] [12] [4] 15
2.2 In this table we show the design specifications and characteristics of PAPER [13; 14] 19

Stellenbosch University https://scholar.sun.ac.za

Nomenclature

Abbreviations

SKA	Square Kilometer Array
NRAO	National Radio Astronomy Observatory
FF	Far Field
NF	Near Field
PA	Phased Array
LOFAR	Low Frequency ARray
PAPER	Precision Array to Probe the Epoch of Reionization
LBA	Low Band Antenna
FT	Fourier Transform
FFT	Fast Fourier Transform
SMA	Semi Major Axis
IFT	Inverse Fourier Transform
PSF	Point Spread Function
DD	Direction Dependence
BD	Baseline Dependence
SVD	Singular Value Decomposition

Stellenbosch University https://scholar.sun.ac.za

Chapter 1

Introduction

1.1 Background

Since human beings started looking skywards, the star-filled heavens have been a source of constant fascination and amazement inspiring us to better understand the cosmos as well as our place in it. For centuries astronomers have looked at skies wanting to know how the universe works; they have since studied planets, stars, galaxies and dust in between. The telescopes that astronomers used were traditionally operated in the visible light which can be seen by the naked eye. Over the last 100 years they have started using instruments that can see other parts of the electromagnetic spectrum, including Radio, Infrared, Ultraviolet and X-ray wavelengths.

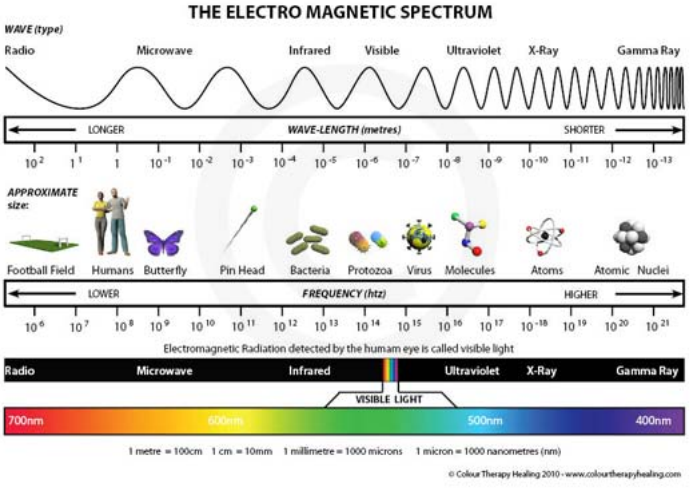

Figure 1.1: The electromagnetic Spectrum. Image Credit: *NRAO*

The radio band represents wavelengths roughly from millimeters to kilometers

Stellenbosch University https://scholar.sun.ac.za

as depicted in the electromagnetic spectrum in Figure 1.1 and radio telescopes are the antenna elements used to observe and map the skies at these frequencies [15].

The basic figures of merit of any telescope are resolution, collecting area, dynamic range, image fidelity and survey speed. The resolution [6] is a measure of how much detail can be observed and the ability to distinguish the source, the equations given by (1.1.1) where λ is the wavelength and D is the diameter of the telescope. Interestingly enough, the resolution of a telescope does not only depend on the diameter, but on the ratio of wavelength to size. This means for radio telescopes operating in the radio band from millimeters to kilometers as compared to optical telescopes operating in visible light (roughly 360 -760 nm); Radio telescopes would need to be a thousand to millions of times larger than optical telescopes to achieve the same resolution. From the equation below we can see why radio interferometers are used instead of single element telescopes, it is because resolution also depends on frequency. At lower frequencies relatively large antennas are needed in order to achieve satisfactory resolution, which is why in an array a baseline is used as an antenna array's longest dimension.

$$\theta \approx \frac{\lambda}{D}. \tag{1.1.1}$$

The collecting area is of equal significance, it is the actual surface area of the antenna and determines the sensitivity of the instrument so that very faint radio signals can be obtained. An antenna array synthesizes a large telescope, but the physical area of the synthesized telescope is approximately the sum of the small areas of the individual elements and not the area of the synthesized telescope. Sensitivity is inversely proportional to the observation time; the less sensitive the instrument, the more time will be needed to collect the signal [6]. However, in principle an antenna can compensate for low sensitivity by spending more time observing the same source collecting more signal. The dynamic range is the measure of the degree at which imaging artifacts surrounding or around strong sources are suppressed. Image fidelity is a measure of the ability to render the sky accurately. Noting from (1.1.1), telescopes thousands of kilometers in diameter would be needed to achieve satisfactory resolution in the radio band are impractical [16]. It follows that at the band of interest, these figures of merit can not be achieved with single elements and radio synthesis telescopes address this problem with distributed systems.

Through a series of radio astronomical projects aiming to achieve the above mentioned figures of merit, the Square Kilometer Array (SKA) is the recent project. The SKA will comprise of an array of antennas up to 3000 km apart [17]. The main aim of the SKA will be to increase sensitivity of our observations of the radio sky at increased resolution, dynamic range, image fidelity and also minimizing ob-

Stellenbosch University https://scholar.sun.ac.za

servation time [18].

This will be a huge challenge because the SKA will collect a massive amount of data that will need sophisticated supercomputers to process and also the images computed by the radio interferometers will need processing to remove the distortions [19]. These distortions will be from the fact that interferometer arrays have gaps in between, as it is not possible to build telescopes of kilometers in diameter. These gaps in the synthetic aperture are unavoidable and they result in sidelobes in the synthesized beam, making the synthesized image distorted and difficult to interpret [20]. Each source in the map will be adding its own sidelobes and sidelobes from brighter sources will contaminate the faint detail. The second kind of distortions will be produced by the Earth's atmosphere and the electronics in the telescopes themselves. These distortions will cause delays and variations in the signal.

The way in which the radio telescopes are distributed depends on the science goals and also is a function of frequency. At low frequencies the element distribution is very sparse while it is more dense at higher frequencies [8]. This is because of the electrical size of the antenna elements at the frequency of observation. Sparse aperture arrays at frequencies below 500 MHz have best prospects for cost-effective performance. The effective receiving area of dipole-like antenna elements becomes comparable to that of reflector-type antennas and also such elements are practical for astronomical purposes. At frequencies below 500 MHz, the sky noise dominates the signal; while the effective receiving area of a dipole increases as the square of the wavelength $Sensitivity = \lambda^2/2$ [21] [22]. Low frequency arrays normally employ conducting meshes below the elements to reduce ground noise. A wide field of view can be imaged and high sensitivity can be achieved by using beamforming techniques. This means that at lower frequencies arrays will be relatively sparse in comparison to high frequency, because sensitivity of aperture arrays is frequency dependent.

With the understanding that antenna elements that are in close proximity interact electromagnetically and therefore are subject to mutual coupling; the FF Equation (1.1.2) has been used to compute FF values corresponding to the low and high frequency values of LOFAR LBA and PAPER. The resulting Table 1.2 aims to give an idea of which elements can possibly be subjected to mutual coupling. Since mutual coupling does not depend only on the separation distance, but also on the orientation; this table aims to give an idea rather than to precisely distinguish mutual coupling.

$$R = 2\frac{l^2}{\lambda}. \tag{1.1.2}$$

At lower frequencies if the antennas are not sparse enough, electromagnetic interaction between the antenna elements will occur and these antenna elements

Stellenbosch University https://scholar.sun.ac.za

will induce electric currents on each other's surfaces [23]. This effect is known as mutual coupling and its effects are serious as they deform and change the radiation patterns of the elements, change their input impedanceâs and received element voltages. Mutual coupling effects reduce the antenna efficiency and perfomance of the antennas [3]. The effects of mutual coupling are very serious if the spacings between the antennas are small. The mutual coupling needs to be addressed as part of the measurement modeling algorithms in order for celestial objects to be recovered from received signal corrupted by sources of noise. So, even for sparse low frequency arrays the FF region of each antenna element is much larger; resulting in closely spaced elements which could lead to mutual coupling. It is also important to note that mutual coupling is not in general an undesired phenomena, as it has its advantages; but for this specific case it is undesired.

In this study we consider two SKA related antenna elements, PAPER and LOFAR. These antenna elements are well known and are considered because of the mutual coupling effects that affect them as shown in Table 1.2. For the tabulated values in Tables 1.1 and 1.2, the symbols B_{min}, B_{max}, R_{min} and R_{max} will be used. The symbols B_{min} and B_{max} are representations of the minimum and maximum separations between the antenna elements. Similarly the symbols R_{min} and R_{max} indicate the computed FF distances where R_{min} is the FF distance of an antenna element as computed from the lower frequency f_{low} and R_{max} is for the high frequency f_{high}. The given FF values were computed using (1.1.2), using the details given in Table 1.3. Tables 1.1 and 1.2 show the minimum and maximum baselines of the antenna arrays and also computed FF measurements.

Table 1.1: Minimum and maximum baseline between antenna elements [8] [9].

Antenna Type	B_{min}	B_{max}
PAPER	8 m	300 m
LOFAR	2.4 m	81 m

Table 1.2: Computed FF values for each antenna element [8] [10].

Antenna Type	R_{min}	R_{max}
PAPER	7.70 m	15.54 m
LOFAR	1.56 m	4.18 m

For low frequency arrays even though the elements are sparsely distributed, mutual coupling is a problem especially if the elements are closely spaced. Clearly,

Stellenbosch University https://scholar.sun.ac.za

Table 1.3: The required characteristics of the two antenna arrays in order to compute FF values for each antenna element

Antenna Type	Dimensions
PAPER	
	f_{low} = 100 MHz
	f_{high} = 200 MHz
	Dipole length = 1.32 m ≡ 0.637 m per arm
	l = 3.414 m
	R_{min} = 7.70 m
	R_{max} = 15.54 m
	B_{min} = 8 m
	B_{max} = 300 m
LOFAR (LBA)	
	f_{low} = 30 MHz
	f_{high} = 80 MHz
	Dipole length = 2.8 m ≡ 1.38 m per arm
	l = 1.95 m
	R_{min} = 1.56 m
	R_{max} = 4.18 m
	B_{min} = 2.14 m
	B_{max} = 81 m

if we were to consider antenna arrays like KAT7 we would not encounter mutual coupling because of the frequency of observation of these elements.

Since mutual coupling as explained above results in distorted radiation patterns, it is not the only reason that leads to nonidentical radiation patterns. For antenna elements to have non-identical radiation patterns, one of two cases must exist. The first case is if the antenna elements themselves are different. This case is possible for arrays used in Very Long Baseline Interferometer (VLBI), where different antenna elements are combined together to form an interferometer. The second case would be when two identical antenna elements are close to each other in such a way that they are in each other's FF.

LOFAR is an interferometer array which is based primarily on the principles of phased arrays. The LOFAR telescope is a combination of two antenna arrays, Low Band Antennas (LBAs) and High Band Antennas (HBAs) which are operating in the frequency band 30-240 MHz. The LBAs operate at 30-80 MHz while the HBAs operate at 120-240 MHz [24][25]. Our interest in LOFAR for this study are the LBAs, They are grouped into stations such that each station has 96 dual-polarized inverted v-shaped dipoles. The maximum baseline within a station is 81 m and the minimum baseline is 2.4 m [8]. For this work, the focus is to extract

Stellenbosch University https://scholar.sun.ac.za

mutual coupling between the antenna elements within stations. So, we have simulated using FEKO a LOFAR LBA-like antenna array (randomly distributed) and aim to extract the mutual coupling effects. However, the simulations are not a replica of the LOFAR LBAs, but are alike in terms of physical characteristics and operation frequencies.

Secondly, we consider PAPER, which also has non-movable parts and its elements are electronically linked to form one large telescope. PAPER is made up of two distinct arrays located at the South African SKA site in the Northern Cape, South Africa and at the NRAO site in Green Bank, West Virginia [10]. The South African site is used for science observations while PAPER in NRAO is used for engineering investigations. PAPER is operating in the frequency range 100-200 MHz and is made of copper crossed dipoles that are encaved between two thin small aluminum disks about 0.6 m above a rectangular reflector [13]. The minimum baseline for PAPER is 8 m and 300 m is the maximum baseline and the aim of this study is to extract mutual coupling between these elements.

The visibility function given by:

$$\mathbf{V}_k(u,v) = \iint \mathbf{A}_k(l,m)\mathbf{I}(l,m)e^{-2i\pi(ul+vm)}dldm, \tag{1.1.3}$$

is different for every baseline k; this baseline dependency breaks down the Fourier relationship of the visibility function $\mathbf{V}_k(u,v)$ and the intensity function $\mathbf{I}(l,m)$. The algorithm to be implemented in this work suggests a solution for this problem and will be fully discussed in the coming chapters. An algorithm, the A-Stacking aims to address the baseline-dependent direction-dependent effects by $'stacking'$ the image domain into a set of apparent skies and then FFT the apparent skies to obtain a set of visibilities [3]. The obtained set of visibilities are degridded to yield a series of visibilities that are summed to give the desired visibilities. The simulations of these arrays will then be used to calculate the cost effectiveness of this algorithm. There are other effects, but for the purposes of this work we will idealize them; but they need to be kept in mind when considering the complete measuring process.

1.2 Problem Statement

The aim of this work is to investigate how the A-Stacking algorithm addresses the problem of non-identical antenna patterns. Specific known antenna elements such as PAPER and LOFAR will be used to simulate the effectiveness of this calibration algorithm.Also, we implement the $Högbom$ CLEAN algorithm on both point-like sources and extended sources and present its performance.

Stellenbosch University https://scholar.sun.ac.za

1.3 The Document Outline

The hierarchy of this thesis is arranged such that all the necessary terminology and tools needed for the understanding of the work discussed in this thesis are covered in the early chapters. Chapters 2 and 3 contextualize the study by fully discussing the most relevant literature available on the subject matter. This content is presented in sections; Chapter 2 fully examines the antenna elements and antenna characteristics. The antenna elements are simulated using FEKO and mutual coupling is discussed. In Chapter 3, literature review pertaining to the full understanding of imaging for the scope of this work is fully discussed.

Chapter 4 builds up on the previous chapters and introduces deconvolution and finally the implementation of the *Högbom* CLEAN algorithm. The clean algorithm is implemented for both point-source like structures and extended source, the performance of the *Högbom* clean is investigated and discussed. Chapter 5 fully discusses the A-Stacking algorithm; this chapter uses the ideas and simulations from the early chapters to calculate the cost effectiveness of the algorithm. The final Chapter (Chapter 6), discusses the results obtained for the A-Stacking algorithm and the *Högbom* CLEAN. This chapter presents the analysis and summary of the implementation of the simulated sky to the end of Chapter 5.

Stellenbosch University https://scholar.sun.ac.za

Chapter 2

Antenna elements

2.1 Introduction

This chapter gives a fundamental literature review for the antenna simulations part of this thesis. A background review on the basic antenna properties needed for the understanding of this work, requirements, design and related issues for LOFAR and PAPER are developed. The above mentioned arrays are some of the important pathfinders and precursors of the Square Kilometer Array (SKA) in order to demonstrate the capabilities of phased aperture arrays. Such telescopes are useful in paving the way and help develop solutions for imaging and calibration issues that are relevant to the SKA. The first section defines an antenna, antenna array and explains their basic properties and also defines mutual coupling. The second section involves the discussion of LOFAR and PAPER arrays and shows the simulated LOFAR-like and PAPER-like antennas.

2.2 Antennas

Waveguides and transmission lines are generally used for signal transmission in the form of guided electromagnetic waves from a source to a load. Antennas on the other hand are devices which may be used to transmit signals in the form of unguided waves from the source to the load. The figures below show the difference between guided and unguided connections [26].

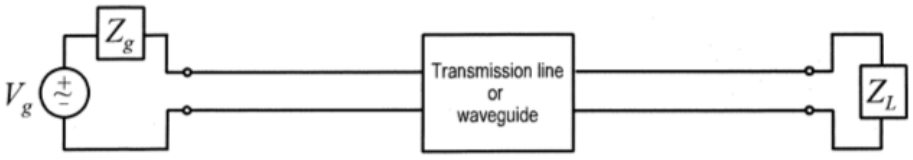

Figure 2.1: An illustration of a guided wave connection [1].

Stellenbosch University https://scholar.sun.ac.za

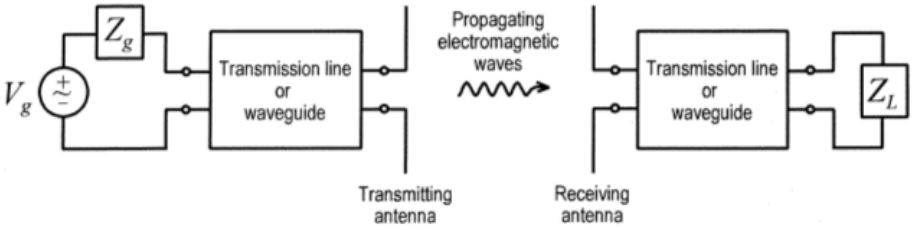

Figure 2.2: An illustration of an unguided wave connection [1].

It would be sufficient to first define an antenna before discussing its parameters. An antenna can be loosely defined to be a device for converting electromagnetic radiation in space into electrical currents in conductors or the other way around [27]. This means that radio telescopes are also antennas as they convert electromagnetic signals from the faraway radio sources into electrical currents in conductors. The reciprocity theorem tells us that we can treat them as transmitters as well as receivers [26; 28; 29].

2.3 Antenna Properties

Having defined what an antenna is, it then follows to define the antenna properties or characteristics that will be needed for the remainder of this work and also the terminology that will be frequently mentioned from here onwards.

2.3.1 Radiation Pattern

The radiated power by the antenna element is distributed over the surrounding regions which are classified as the Near Field (NF) and Far Field (FF) where the NF is the immediate region surrounding the antenna. The radiation pattern is a function of spatial angle and radial distance and can either be classified as a field pattern (in terms of the field intensity) or power pattern (in terms of the power)[30; 1]. Therefore, a radiation pattern is a graphical representation of how an antenna radiates in its surroundings.

2.3.2 Near and Far Field Regions

The terms FF and NF describe the fields around any electromagnetic-radiation source. The neighborhood of the radiating element is then categorized into two regions. The FF region is dominated by radiated fields with the electric fields orthogonal to the magnetic fields and direction of propagation, as with plane waves. A distinction has to be made as to where the FF region begins or where the

Stellenbosch University https://scholar.sun.ac.za

NF ends. The regions are a function of antenna size and the frequency of operation, where D represents the longest antenna dimension and λ is the wavelength of operation. Figure 2.3 shows how the FF and the NF are classified around the antenna [23; 31].

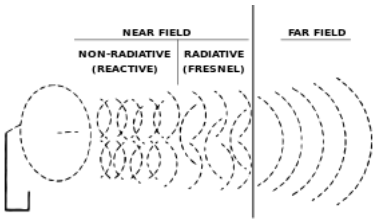

Figure 2.3: A schematic representation of the near and far-field regions [2].

The boundary between these regions can be approximated by [26].

$$R > 2\frac{D^2}{\lambda}, \qquad R \gg D. \tag{2.3.1}$$

2.3.3 Gain and Directivity

The directivity of an antenna element measures the degree to which the radiated radiation is concentrated in a single direction. This is a measure of power density the antenna elements radiate in its direction of strong radiation in comparison to the power density of an ideal isotropic antenna. A highly directional antenna implies or assumes that the direction of the point of interest is known. In order to define the gain of an antenna, another term known as the radiation efficiency needs to be defined. It is a measure of how much of the power that drives the antenna is actually radiated into free space. The more power radiated, the more efficient is the antenna [1]. The gain of an antenna is the product of its directivity and its radiation efficiency. Antennas with high gain do not imply that we are getting more power out than power that is put instead we get more power towards a certain direction [6].

$$D(\theta,\phi) = \frac{U(\theta,\phi)}{U_{ave}} \tag{2.3.2}$$

Equation (2.3.2) computes the ratio of the radiation intensity in a particular direction to the average radiation intensity [26], $U(\theta,\phi)$ is the power radiated in a specific direction per unit solid angle (radiation intensity) and U_{ave} average radiation intensity.

Stellenbosch University https://scholar.sun.ac.za

2.3.4 Mutual Coupling

The electromagnetic interaction between the antenna elements of an array when the antenna elements are in each other's near field is known as mutual coupling. Mutual coupling describes the absorption of energy by one antenna receiver when another antenna in close proximity is in operation [1] [27]. It is undesirable because energy that should have been absorbed or radiated by one antenna is absorbed by the nearby antenna [23] [28] ;affects the terminal impedances and reflection coefficients and consequently the array gain. Hence, mutual coupling reduces the performance and efficiency of the antenna in both receive and transmit modes.

The FEKO simulations computed throughout this work are in transmit mode although the real antennas are in receive mode and this is allowed because of the reciprocity theorem. In this work, mutual coupling is undesired as it distorts the beams of antennas. However, outside of this work mutual coupling is not always considered undesirable as it can be used to increase bandwidth [30]. For both the simulated arrays, the bottom dipole is excited; corresponding to the x-axis with 75Ω. The reflection coefficients extracted are to show mutual coupling. Figure 2.11 shows the variation of reflection coefficients from antennas that are in close proximity.

Figures 2.4 and 2.5 show randomly distributed elements consisting of 11 LOFAR-like and PAPER-like antennas. The distances are in such a way that the elements are in close proximity. Figure(s) 2.6 and 2.7, show the variations in patterns due to mutual coupling. The next Figure 2.7 shows variation in the reflection coefficients in the PAPER-like randomly distributed array.

2.4 Dipole Antenna

The most popular and simplest type of radio antenna is a dipole antenna and is used extensively in radio communications because it is among the least expensive antenna elements [1]. A dipole antenna is made up of two wires where the current flows. A dipole antenna response is length dependent and is best resonant at half wavelength. The thickness of the dipole is also very important as it reduces the resonant frequency and makes the antenna more broadband [32; 15]. The selected antenna elements for this work are dipole elements and will be showing the above characteristics in some way.

Stellenbosch University https://scholar.sun.ac.za

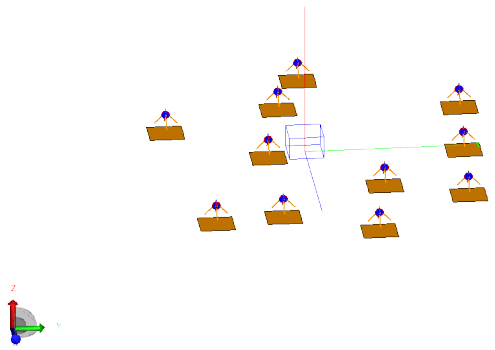

Figure 2.4: Randomly generated LOFAR-like antenna array using FEKO with bottom port excited with 75Ω.

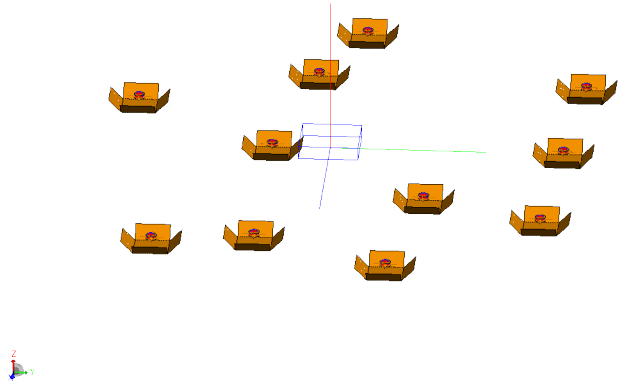

Figure 2.5: Randomly generated PAPER-like antenna array using FEKO, excited at the lower port with 75Ω.

2.4.1 Antenna Arrays

Increasing the length of an antenna increases the gain of that antenna element. However, the notion of increasing the length of an antenna is limited. Increasing the length of a linear antenna above λ causes the linear antenna to lose its characteristics. Side-lobes, back lobes and vestigial lobes start to develop. The goal of achieving high gain can be obtained by using several individual antennas so spaced and phased that their individual contributions add in one preferred direction to give a high gain and directivity and cancel in other undesired direc-

Stellenbosch University https://scholar.sun.ac.za

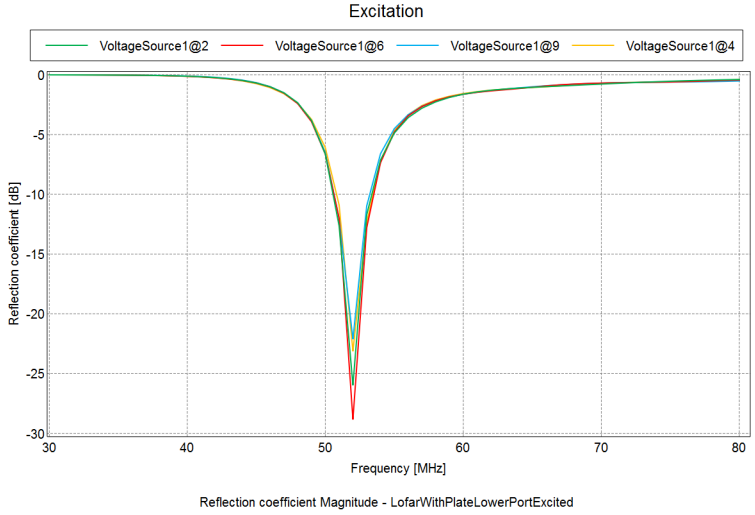

Figure 2.6: Variations in the reflection coefficient for LOFAR element due to mutual coupling effects.

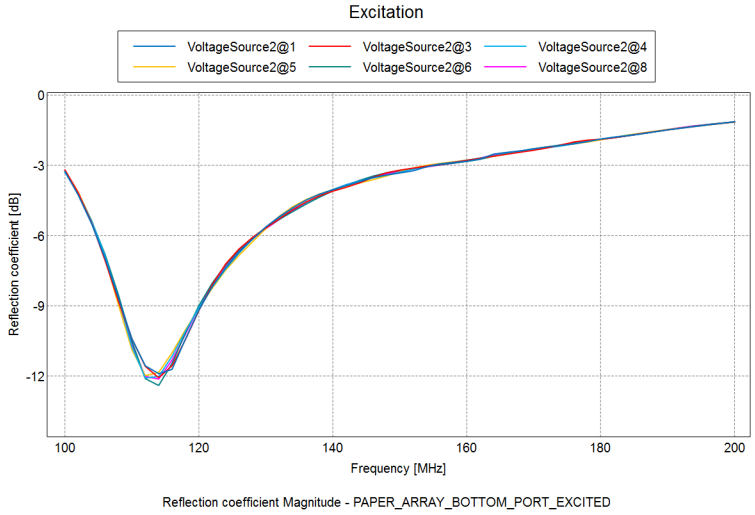

Figure 2.7: Variations in antenna reflection of PAPER element due to mutual coupling.

tions [6]. So the antenna arrays are built with that goal in mind.

2.4.2 The Low Frequency Array Telescope (LOFAR)

The Low Frequency Array (LOFAR) radio telescope is an interferometer array based primarily on the principles of Phased Arrays (PA)'s. This telescope has been developed by the Netherlands Institute for Radio Astronomy (ASTRON) together with industrial parties and a consortium of universities [4; 8]. It is situated mainly in the Netherlands, with a couple of international stations (Germany, France, UK,

Stellenbosch University https://scholar.sun.ac.za

Finland and Sweden). Figure 2.8 shows the core of LOFAR as imaged from the sky.

Figure 2.8: The airial view of the core of LOFAR in Netherlands [3]

The LOFAR telescope operates in the frequency range 30-240 MHz and is divided into two frequency bands, operated by two different antennas, Low Band Antennas (LBAs) and High Band Antennas (HBAs). The frequency range of 30-80 MHz is observed by the LBAs and the range of 120-240 MHz is observed by HBAs with the exclusion of the FM band [12]. The LBAs are dual polarized dipoles in the form of inverted V-shaped crossed dipoles with the arms of the dipoles making an angle of 45°with the ground. The length of each dipole arm is about 1.4 m. The PVC rod is 1.7 m in height from the ground [24] [33]. A string and a spring are used to prevent the dipoles from moving and maintaining the 45°angle with the ground. Figure 2.9 shows a detailed structure of the antenna.

Stellenbosch University https://scholar.sun.ac.za

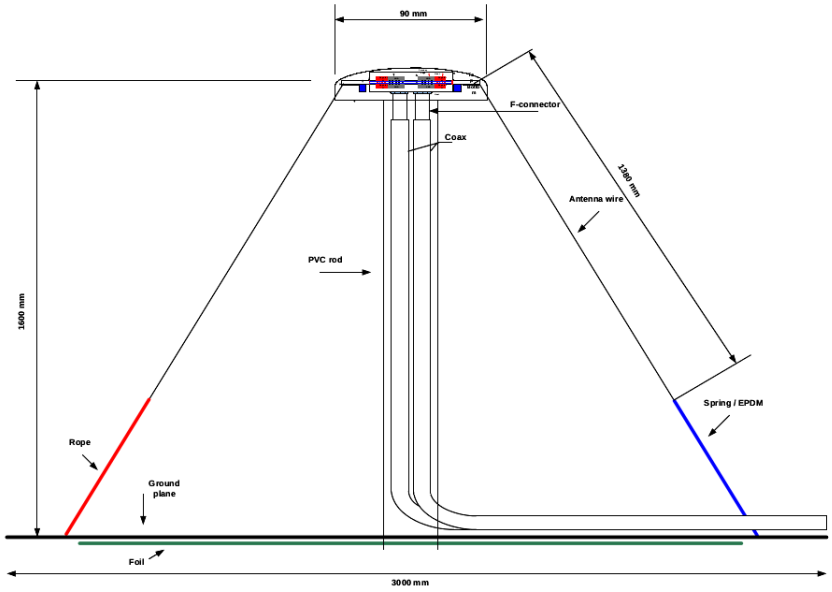

Figure 2.9: The structure of the LOFAR LBA antenna [4].

The two V-shaped orthogonal dipoles are sensitive to two orthogonal linear polarizations and therefore have two wires going down the PVC rod preserving the polarization [34]. The antennas are grouped into stations, such that a LBA station consist of 24 LBAs. The diameter of a LBA station is 81 m with a minimum baseline of about 2.4 m [8]. The spatial distribution of the LOFAR antennas is due to the specifications of the science goals required. The LOFAR configuration is more dense at the core to allow for sensitivity and spreads out in a logarithmic spiral manner for resolution. The signals collected by these antennas are combined by beamforming techniques into a station beam. The basic dimensions and characteristics of a LOFAR LBA antenna are shown in Table 2.1.

Table 2.1: Table showing the design specifications and characteristics of LOFAR [11] [12] [4]

Characteristics of LOFARs LBA	
Antenna height	1.7 m
Dipole length	1.38 m
Frequency range	30-80 MHz
Ground plane	3×3 m
Min baseline	2.4 m
Max baseline	81 m

Stellenbosch University https://scholar.sun.ac.za

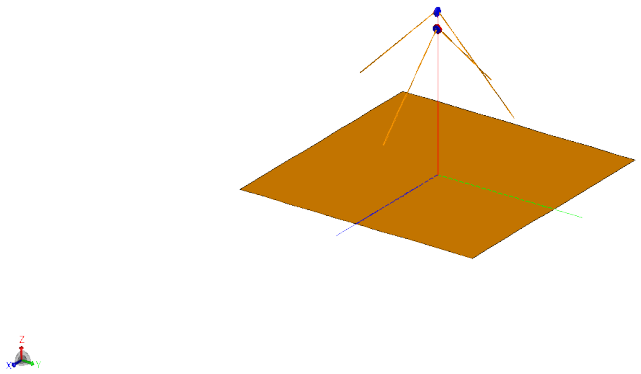

Figure 2.10: The model of the LOFAR-like antenna.

Figure 2.10 is a FEKO model of a LOFAR-like antenna which adopts the physical specifications identical to that of LOFAR. The gap between the inverted V-shaped dipole arms are about $\frac{\lambda}{1000}$, where λ is obtained using the lowest frequency of the operation band. The antenna is excited at the lower port with 75Ω and the lower dipole is along the x-axis at distance z above the ground screen.

Figure 2.11 shows the performance of the antenna at different frequencies, namely 80 MHz and 30 MHz. We see a more directional pattern at frequency 30 MHz as compared to 80 MHz pattern. Again, this is the pattern of a LOFAR-like antenna (two v-shaped cross dipole) with the bottom dipole excited (along the x-axis).

Stellenbosch University https://scholar.sun.ac.za

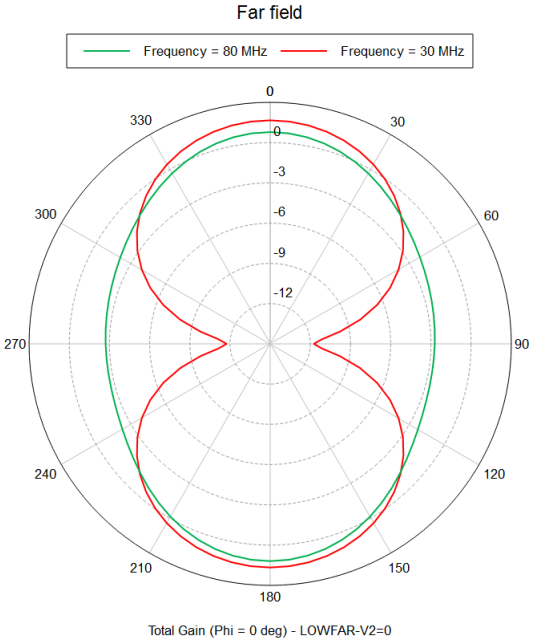

Figure 2.11: The radiation pattern of the LOFAR-like antenna at the edges of the frequency band.

Figure 2.12 shows the reflection coefficient of the antenna. The antenna is best resonant at ≈ 53 MHz which corresponds to its length of ≈ 2.7 m. An antenna is said to be resonant when its input impedance is real, indicating that power is radiated well around that particular frequency and that can be viewed on a frequency plot of S_{11}. A dipole is best resonant at half-wavelength and then thickness also plays a role in decreasing or increasing the resonant frequency [28]. Figure 2.13 shows the impedance of the simulated LOFAR-like antenna, with resonance at about 52 MHz. Figure 2.13 shows the real and imaginary parts of the impedence.

Stellenbosch University https://scholar.sun.ac.za

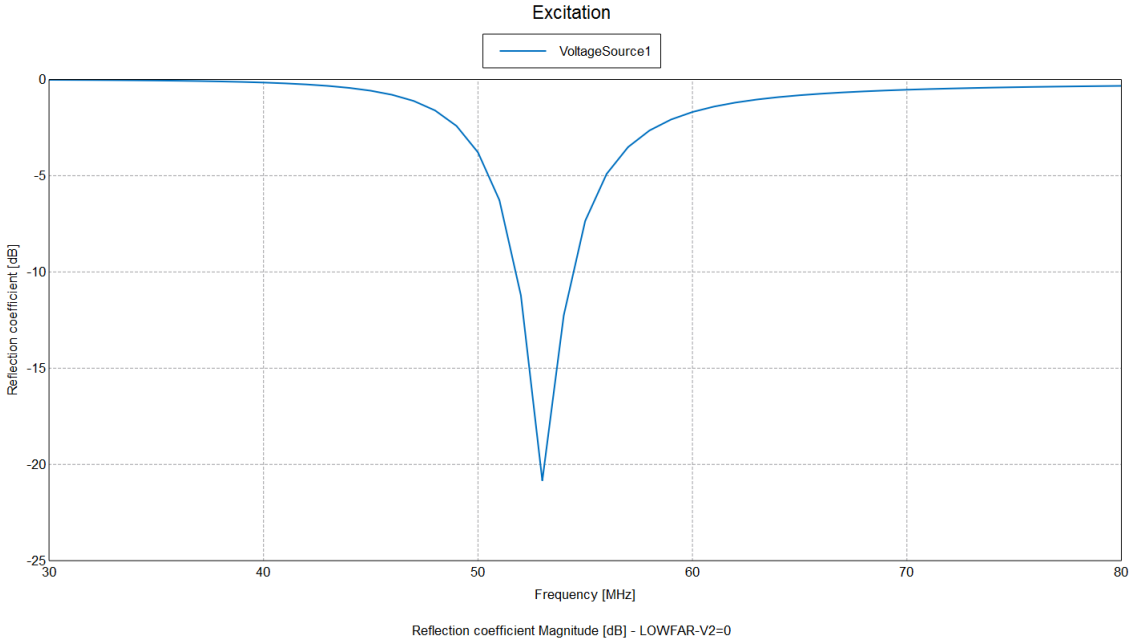

Figure 2.12: The Reflection Coefficient of the LOFAR-like antenna, appearing to be best resonant at half-wavelength.

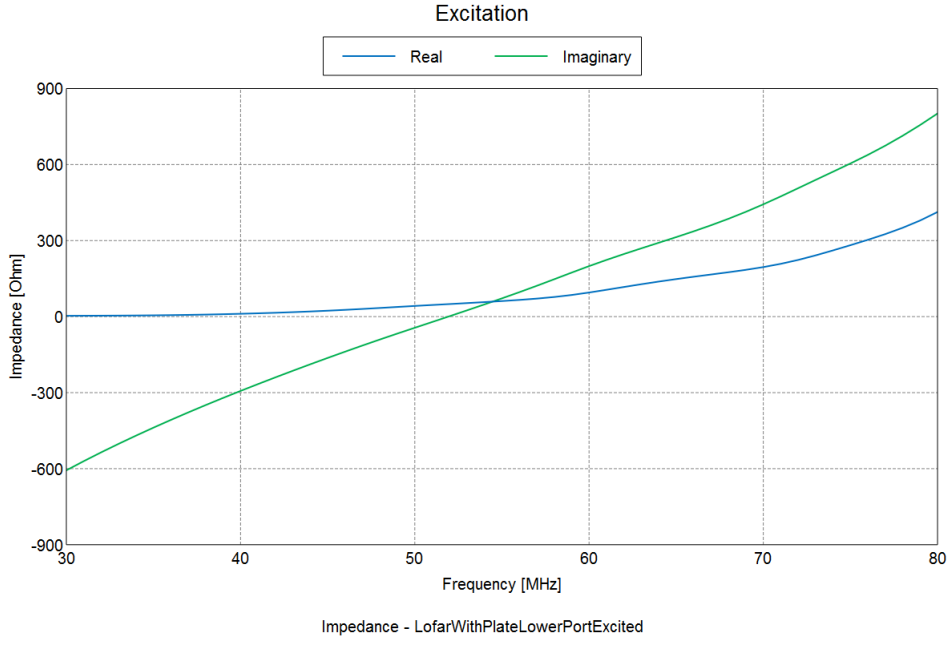

Figure 2.13: Illustration of the real and imaginary impedences of the LOFAR-like antenna element. computed from FEKO.

Stellenbosch University https://scholar.sun.ac.za

2.4.3 Precision Array to Probe the Epoch of Reionization (PAPER)

The Precision Array for Probing the Epoch of Re-ionization is an interferometer array developed to detect the 21 cm emission line of hydrogen from the early universe, when the first galaxies and stars were formed. The epoch of re-ionization (EoR) is an era in time when the inter-galactic medium (IGM) was transforming from being neutral to being ionized due to the radiation from the first galaxies and stars. The main goal of the PAPER experiment is the power spectrum detections in the fluctuations of the neutral hydrogen emission at high redshifts [5].

The design of PAPER consists of broad-band dual polarized non-tracking dipoles with active baluns, coaxial cable transmission, digitization and correlation. The antennas are operated in the frequency range of 100-200 MHz and measures linear polarizations [9; 10]. In the table below, we tabulate some of the specifications of the PAPER array.

Table 2.2: In this table we show the design specifications and characteristics of PAPER [13; 14]

Characteristics of the PAPER in South Africa	
Frequency range	100 - 200 MHz
Number of antennas	128
Minimum baseline B_{min}	8 m
Maximum Baseline B_{maX}	300 m
Frequency f_{low}-f_{high}	100-200 MHz
Longest dimension of the antenna l	$\approx$ 3,838 m

The PAPER has been deployed in a series of phases in South Africa and at the NRAO site near Green Bank, West Virginia. A 32 antenna deployment at the NRAO site near Green Bank is primarily used for engineering investigations and field testing. The South Africa PAPER deployment was initially 16 antennas and now stands at 128, This deployment is primarily for the science observations [35]. Figure 2.14 shows a single PAPER antenna element from the South African deployment.

Stellenbosch University https://scholar.sun.ac.za

The antenna element is based on a sleeved dipole concept, made up of a pair of perpendicularly polarized dipoles that are positioned in between a pair of metal disks at a distance ~ 0.608 m above the rectangular reflective structure [14; 9]. The ground screen is made up of a 2×2 m wooden frame with 0.5×0.5 $inch$ mesh wire serving as a reflecting surface. The reflector side flaps are at 45°. The active balun is mounted directly at the lower disk and the antenna is supported by a PVC pipe [36; 37].

Figure 2.14: A single PAPER antenna from the SKA site in South Africa [5]

The deployment of 4 antenna elements of PAPER in 2005 at the NRAO site near Green Bank, West Virginia marked the beginning of PAPER activities. After continuous improvements to the initial PAPER design, Green Bank now hosts an antenna array of 32 elements [13]. These elements are used to explore the best array configurations for a power spectrum measurement and to improve the global sky model. The deployment of PAPER in South Africa began with the deployment of 16 antennas in October 2009. By April 2010 it has been increased to 32 antennas, then to 64 and ultimately to 128 antennas at the end of 2013.

An identical antenna element, which we refer to as a PAPER-like antenna was simulated in this study making use of some of the specifications of the South African PAPER deployment. The simulations of a PAPER-like antenna were computed using FEKO, Figure 2.15, 2.16, 2.17 representing the built PAPER-like model, the obtained reflection coefficient and the gain patterns. Figures 2.15, 2.16, and 2.17 represent the model of a PAPER-like antenna, reflection coefficient of a PAPER-like antenna and the total gain of one PAPER-like element respectively.

Stellenbosch University https://scholar.sun.ac.za

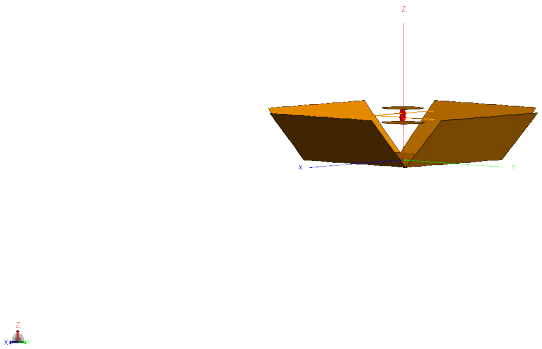

Figure 2.15: The FEKO model of the PAPER-like antenna.

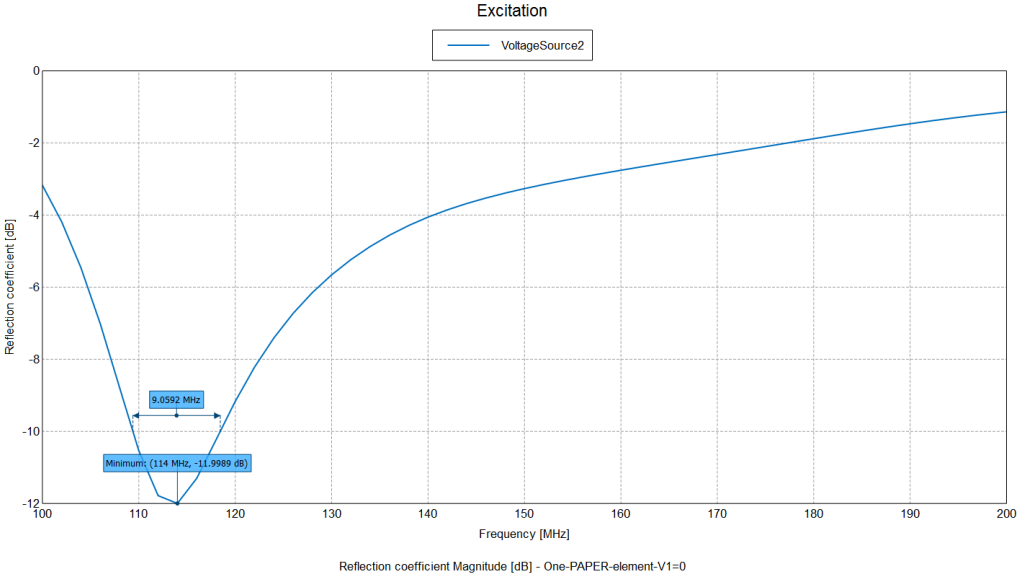

Figure 2.16: The reflection coefficient of the PAPER-like antenna.

From the above images, we see a variation in gain pattern with varying frequency. We also note the reflection coefficient of the PAPER-like model appears to be resonating more at ≈ 114 MHz. This is a horizontal cut of the gain pattern, meaning we are analysing the variations of the pattern along θ with frequency.

2.5 Conclusion

In this chapter the basic and necessary literature review for antennas has been performed. The LOFAR and PAPER-like elements have been simulated and figures illustrating their performances have been shown. The phenomena of mu-

Stellenbosch University https://scholar.sun.ac.za

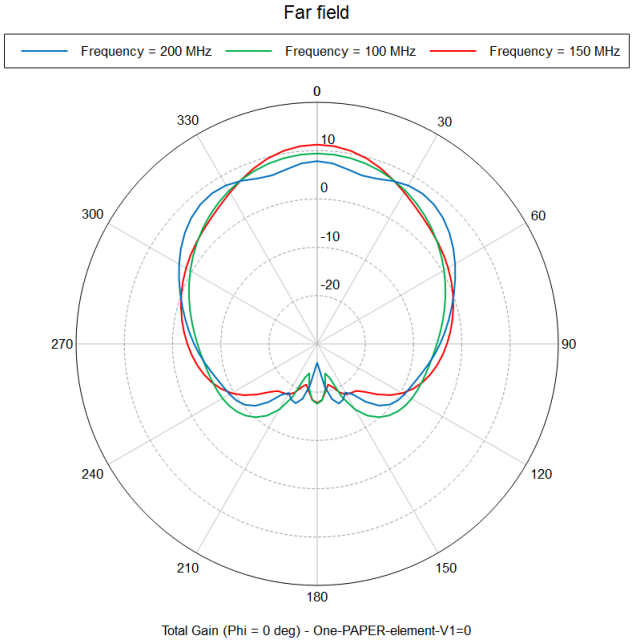

Figure 2.17: The radiation pattern of the PAPER-like antenna.

tual coupling for low frequency arrays like the LOFAR and PAPER have been observed. Mutual coupling has been shown to result in the distortion or variation of the reflection coefficients of antenna elements which are in close proximity.

The simulation of these antenna elements (LOFAR-like and PAPER-like) does not, and is not aimed at trying to reproduce the LOFAR and PAPER elements. The direction-dependent effects are due to a number of effects, but for this work we are interested in effects due to mutual coupling. The ideas drawn from this chapter will be used when the DD matrix is computed, which will be used for A-Stacking; which is yet to be discussed.

Stellenbosch University https://scholar.sun.ac.za

Chapter 3

Radio Interferometers and Aperture Synthesis

3.1 Introduction

This chapter reviews the literature for understanding the imaging part of this thesis. The imaging part of this work will be motivated from angular resolution all the way to the visibility weighting functions. Graphs will be simulated to illustrate some of the important points to be noted in this work. The details of earth rotation and aperture synthesis will be discussed fully, and the visibility function, intensity distribution function and the uv-coverage will be explained. At the end of the chapter, concluding remarks are provided to wrap up the chapter.

3.2 The Quest for Angular Resolution, θ.

The angular resolution of a telescope is among the basic and most important figures of merit as described in Chapter 2. The rising interest in the details of astronomical sources has stimulated the interests in using interferometers. Interferometry is a technique which uses two or more antenna elements (telescopes in this instant) to observe astronomical sources yielding greater resolution in comparison to observations performed with a single element [6]. An interferometer is the array itself together with the electronics that are used to synthesize the detected signals by the antennas. The Very Large Array (VLA) is shown in Figure 3.1 to illustrate the synthesized aperture and show a typical interferometer [25]. It is made up of dishes with a diameter of 25 m which span a maximum baseline of 36 km. Together, these antennas synthesize an aperture of up to 36 km wide.

The motivation for interferometers is that the angular resolution is directly proportional to the ratio of the wavelength of operation over the diameter of the antenna element. The diameter D, of the synthesized aperture is taken to be the

Stellenbosch University https://scholar.sun.ac.za

Figure 3.1: Image showing the synthesized aperture from the VLA. Credit: NRAO

largest separation between two elements, called the baseline. The synthesized beamwidth is given by Equation (3.2.1) [6].

$$\theta = \frac{\lambda}{D}. \tag{3.2.1}$$

3.3 The 2-Element Interferometer Conceptualization

A two-element interferometer comprises of two antenna elements, antenna i and antenna j, separated by a vector $b_{i,j}$ called the *baseline* as shown in Figure 3.2.

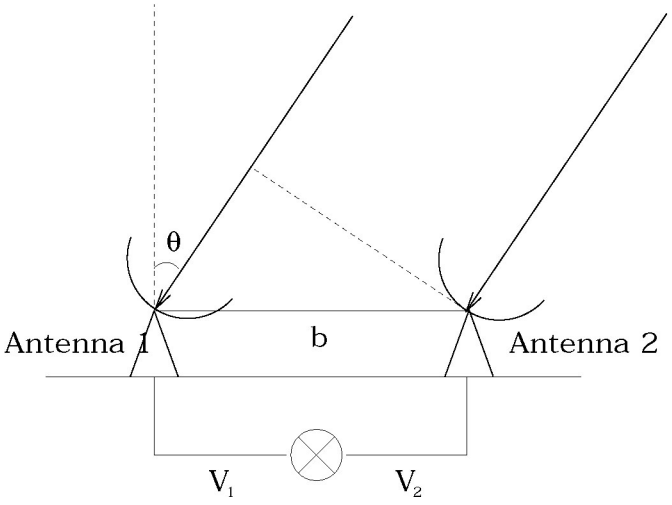

Figure 3.2: Figure showing a two element interferometer [1]

Stellenbosch University https://scholar.sun.ac.za

The antenna elements receive radiation from far away astronomical sources in the form of plane waves and the source direction is denoted by the unit vector $\hat{s}$. The position of the astronomical source in the sky plays a pivotal role in determining the delay between the signals received by the antennas. Due to the physical separation of the antennas by $\vec{b}_{i,j}$, the antenna elements will not receive the signal at the same time. There will be a delay in the time taken for the signal to arrive at both antennas, called the *geometric delay* $\tau_{i,j}$. The extra time taken by the wave before arriving on the second antenna is given by Equation (3.3.1) [38].

$$\tau_{i,j} = \frac{\vec{b}_{i,j} \cdot \hat{s}}{c}.. \tag{3.3.1}$$

Since the sky has a number of sources, each source would have a different geometric delay, because the directional unit vectors would be different for every source. Each antenna would be detecting signal from each source and thus would be detecting the sum of the signals. The signals can be distinguished by correlation, where correlation is a method used to evaluate how much is one signal present in other signals [25; 39]. Figure 3.2 shows a 2-element interferometer, showing signal at an angle θ between antenna i and antenna j separated by baseline b.

3.4 Earth Rotation Aperture Synthesis

The method of aperture synthesis combines the principles of interferometry and the rotation of the Earth. The Earth is rotating about its axis and also orbits the sun. Aperture synthesis uses the projected baselines and the Earth's rotation to fill the uv-plane. The distance between the two antennas forms a baseline, then the projected baseline traces a semi-circle over a period of time as depicted in Figures 3.4 and 3.6 [40].

The length of the uv-tracks depends on the wavelength and also the integration time. In this specific example the observer's latitude is taken to be 35° and the observation time is taken to be 12 hours with a source declination of 90°. It can further be shown that the uv-tracks vary in shape with changing declination. At declination of 90° we observe circular traces and these degenerate into ellipses with changing declination until they are straight lines at 0°. The uv-tracks depends on the wavelength and also the observation time h (hour angle).

Stellenbosch University https://scholar.sun.ac.za

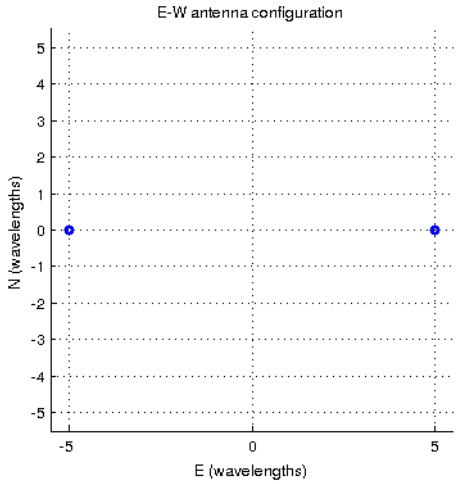

Figure 3.3: The antenna positions on the ground for an East-West interferometer.

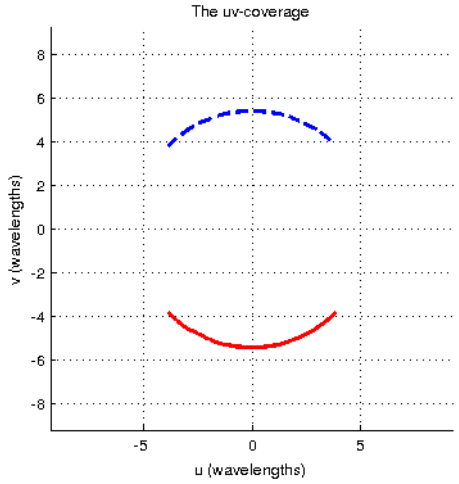

Figure 3.4: The uv-tracks for a 90 degrees declination as traced by the projected baseline with time of 6 hours.

3.5 The co-ordinate system and antenna spacings

Without losing generality, our discussion can be restricted to a single frequency ν with λ as the corresponding wavelength. The geometric delay can be written as the number of wavelengths, as given by Equation (3.5.1)[38].

$$\tau_{i,j}\nu = \frac{b_{i,j}\cdot\hat{s}}{\lambda}. \tag{3.5.1}$$

Having found the distance between the antennas in wavelengths, the complex phase shift between the signals is given by $e^{i\theta}$, where θ is the angle swept

Stellenbosch University https://scholar.sun.ac.za

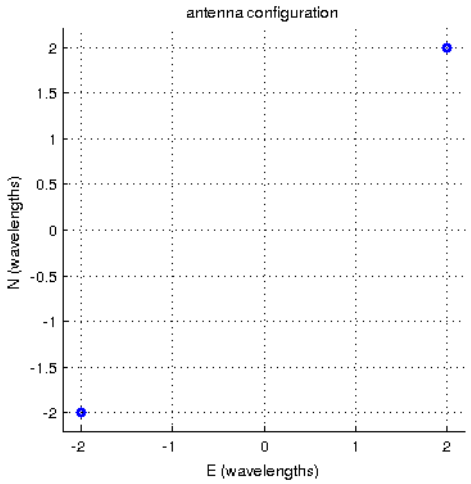

Figure 3.5: The antenna positions on the ground for a SW-NE configuration.

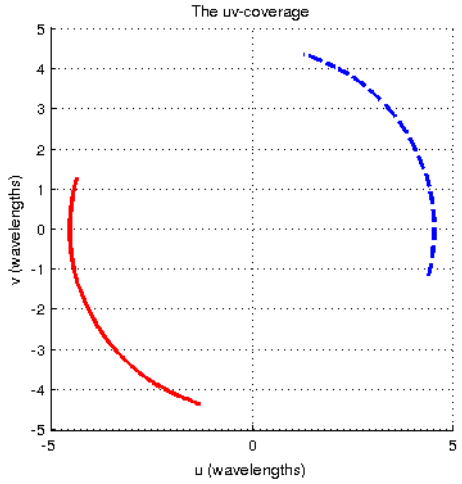

Figure 3.6: The uv-tracks for a 90 degrees declination as traced by the projected baseline over a time of 6 hours and antennas positioned in a SW-NE configuration.

out by the wave from antenna i to j [41; 6]. Using the fact that θ is 2π times the number of wavelengths, the phase is given by Equation 3.5.2.

$$\triangle\phi = e^{-2\pi i \tau_{i,j} \nu}. \tag{3.5.2}$$

In order to measure what the interferometer measures, we confine our measurements to a plane and then define some variables. We first define the coordinates representing the baseline length in units of wavelength in Equation 3.5.3:

Stellenbosch University https://scholar.sun.ac.za

$$\frac{\vec{b}}{\lambda} \equiv (u, v, w), \tag{3.5.3}$$

where u is the east-west direction, v is the north-south and w is in the phase reference direction . Similarly, the source direction $\hat{s}$ can be split as Equation 3.5.4.

$$\hat{s} \equiv (l, m, n = \sqrt{1 - l^2 - m^2}), \tag{3.5.4}$$

where l is East-West direction, m is the North-South direction and the n component is from the fact that $\hat{s}$ is of unit length. A schematic visualization of these variables is shown in Figure 3.7. Using the above components, the response of a baseline as a function of (u, v, w), is called the $visibility$ function and it can be computed by integrating over all of the source intensity **I** on the sky as a function of (l, m, n) as depicted by figure 3.7 [42].

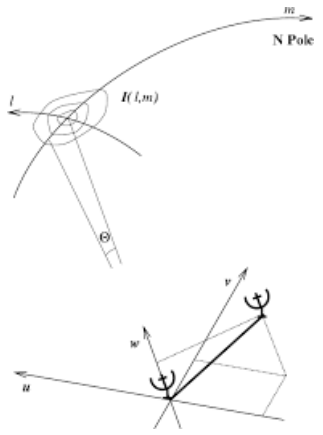

Figure 3.7: The sky and uvw coordinates [6]

3.6 The Visibility, Intensity Distribution Function and the uv-Coverage

The response of an interferometer as a function of (u, v, w) which is a complex function given by Equation (3.6.1) having assumed flat sky approximation, we obtain Equation (3.6.1).

Stellenbosch University https://scholar.sun.ac.za

$$V_\nu(u,v) = \iint A_\nu(l,m) I_\nu(l,m) e^{-2\pi i(ul+\nu m)} dl dm. \tag{3.6.1}$$

The term $A_\nu(l,m)$ inside the integral is the antenna primary beam response as a function of the sky direction (l,m) if the antenna patterns are the same, otherwise it is the product of the antennas voltage patterns. The product inside the integral is called the perceived sky as it is seen through the filter of a primary beam. In this form, the visibility function $V_\nu(u,v)$ can be computed by taking the Fourier Transform (FT) of the perceived sky and the result would be computed in the uv-plane [43].

The uv-plane is sampled at various baselines in the array because of the gaps in an interferometer array. The sampling function can be obtained from the array configuration, because the baselines that result from the array configuration will only give measurements at specific positions in the uv-plane. We also note that the sky brightness is real valued because there are no complex fluxes; for each antenna pair two samples are obtained, one at (u,v) and another at $(-u,-v)$ and the relation is the complex conjugate $V^*(u,v) = V(-u,-v)$. This relation can be explained in two ways [44].

First, since the sky brightness is real valued in the image domain, its FT gives a Hermitian function in the visibility domain. A Hermitian function is a function that has an even real part and an odd imaginary part. Second, when computing the baseline for two antennas on a coordinate system, a reference antenna has to be chosen. However, the baseline is the same from point i to j and from j to i but with a negative direction. Therefore, for one baseline we obtain two u,v points [45]. The gaps between antenna elements in an array implies that the visibility function is the product of the uv-plane and the sampling function. The sampling function is a function that has values only for the measured parts of the uv-plane and therefore the uv-coverage is the uv sampling function.

Taking the Inverse Fourier Transform (IFT) of the sampled uv-plane which is the uv-coverage, we obtain the synthesized beam or the point spread function (PSF) also known as the dirty beam. The synthesised beam will have prominent sidelobes because data is lost when sampling the uv-plane [46]. The existence of side lobes in the synthesised beam results in a badly recovered sky distribution, such that the recovered sky will have too much artifacts. This idea is equivalent to convolving the true sky with the IFT of the sampling function because the IFT of the sampling function is the synthesized beam. The resulting image will be heavily distorted with noise and is called the synthesised map or dirty image.

Stellenbosch University https://scholar.sun.ac.za

3.6.1 More Details About The uv-Tracks and uv-Coverage

As the interferometer or a pair of antennas track a source in the sky through an interval of hour angles, the projected baselines vary in orientation and in magnitude. The locus of the spatial frequencies (u, v) is an ellipse of semi-major axis (SMA) given with the eccentricity given by $\cos(\delta)$ centered at $u = 0$, $v = B_z \cos(\delta)$.

$$SMA = (B_x^2 + B_y^2)^{\frac{1}{2}}.[6] \tag{3.6.2}$$

The interferometer measures the complex visibility function, which is the Fourier components of the sky distribution function having spatial frequency equal to the projected baseline lengths. The components of the spatial frequency can be computed at various hour angles H as shown by equation (3.6.3) where δ is the declination of the source [6].

$$\begin{aligned} u &= X\sin(H) - Y\cos(H) \\ v &= Z\cos(\delta) - X\sin(\delta)\cos(H) - Y\sin(\delta)\sin(H) \end{aligned} \tag{3.6.3}$$

The following definitions are made with reference to figure 3.8.

X is the length of the projected baseline in wavelengths at $H = 0°$, $\delta = 0°$

Y is the length of the projected baseline in wavelengths at $H = -6°$, $\delta = 0°$

Z is the length of the projected baseline in wavelengths at $\delta = 90°$ [6].

It is noted that at higher declinations, the loci are nearly circular and the uv-coverage is reasonably symmetric. As the declination decreases towards zero, moving closer to the equator, the circular structure degenerates into ellipses and then into straight lines. Therefore, as the declination decreases the uv-plane is compressed along the v-axis. For simplicity, the baseline elevation angle is assumed to be zero since the measurements are made on a flat uv-plane. The azimuthal angle is measured from North towards East. The uv-coverage is computed by Equation (3.6.4) which is the matrix form of Equation (3.6.3).

$$\begin{bmatrix} u \\ v \\ w \end{bmatrix} = \begin{bmatrix} \sin(H) & \cos(H) & 0 \\ -\sin(\delta)\cos(H) & \sin(\delta)\sin(H) & \cos(\delta) \\ \cos(\delta)\cos(H) & -\cos(\delta)\sin(H) & \sin(\delta) \end{bmatrix} \begin{bmatrix} X \\ Y \\ Z \end{bmatrix} [6] \tag{3.6.4}$$

$$\begin{bmatrix} X \\ Y \\ Z \end{bmatrix} = D \begin{bmatrix} \cos(\mathscr{L})\sin(\mathscr{E}) - \sin(\mathscr{L})\cos(\mathscr{E})\sin(\mathscr{A}) \\ \cos(\mathscr{E})\sin(\mathscr{A}) \\ \sin(\mathscr{L})\sin(\mathscr{E}) + \cos(\mathscr{L})\cos(\mathscr{E})\cos(\mathscr{A}) \end{bmatrix} [6] \tag{3.6.5}$$

Stellenbosch University https://scholar.sun.ac.za

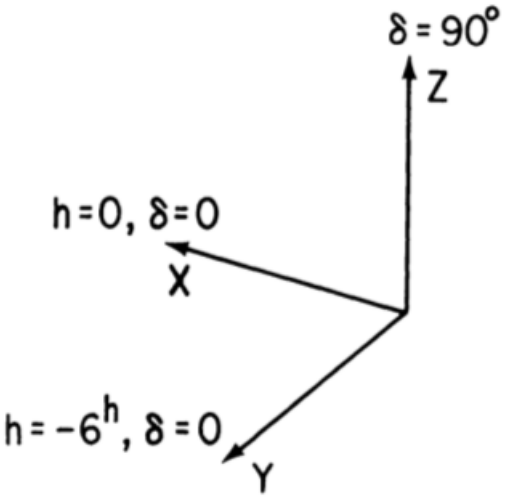

Figure 3.8: This is the adopted coordinate system [7].

The variables $\mathscr{E}$, $\mathscr{A}$ and $\mathscr{L}$ are the baseline $elevation$, $azimuth$ angles and the observers $lattitude$ angle. To further illustrate the above discussed concepts, a simple interferometer array has been simulated at 300 MHz with the VLA-like antenna array as depicted in Figures 3.9, 3.10 and 3.11 respectively. The VLA-like array used here, like the LOFAR-like and PAPER-like antenna arrays simulated in the preceding Chapter is not in anyway an attempt at replicating the VLA and any of it's configurations. This is toy array with a Y looking structure.

These plots show how the eccentricity of the ellipses vary with varying declination angle and how the uv-tracks correspond to baseline lengths and frequency. The baselines track circles at $\delta = 90°$ and degenerate to straight lines at $\delta = 0°$. The next step of moving from the uv-coverage to the dirty beam and similarly to the dirty map requires knowledge of the Fourier Analysis.

Stellenbosch University https://scholar.sun.ac.za

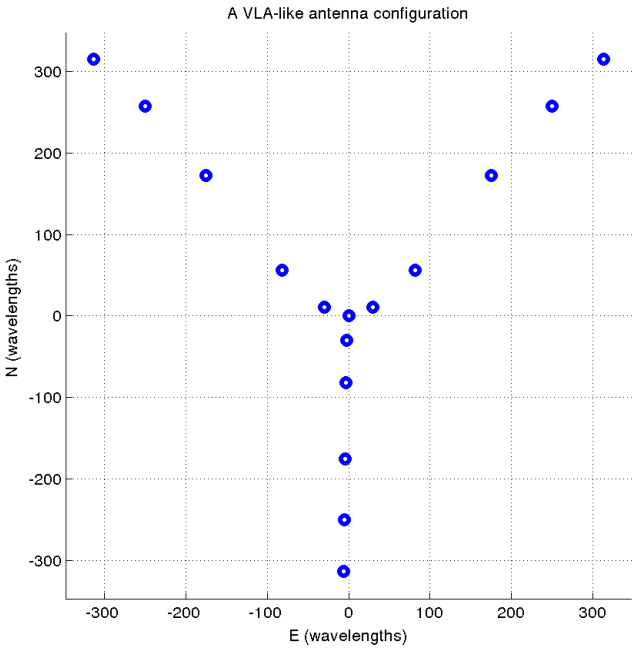

Figure 3.9: Antenna configuration of a VLA-like interferometer.

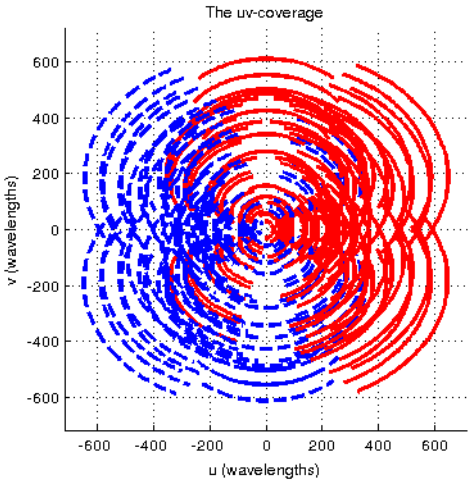

Figure 3.10: The uv-coverage for a 6 hours observation of a source at 45° declination with the VLA-like interferometer.

3.7 The Synthesised beam and the weighting functions

The shape of the dirty beam can be fine tuned by applying the tapering and weighting functions for purposes of sensitivity and resolution and those func-

Stellenbosch University https://scholar.sun.ac.za

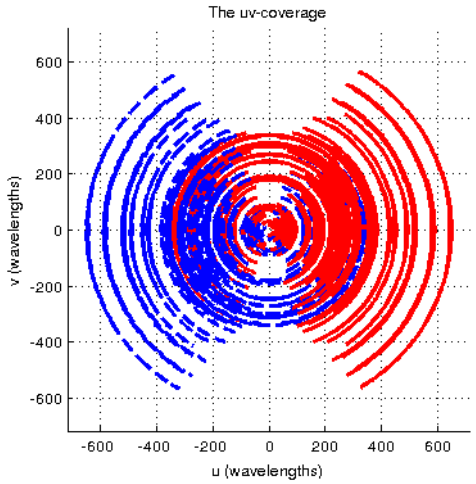

Figure 3.11: The uv-coverage at declination 90° for a 6 hour observation.

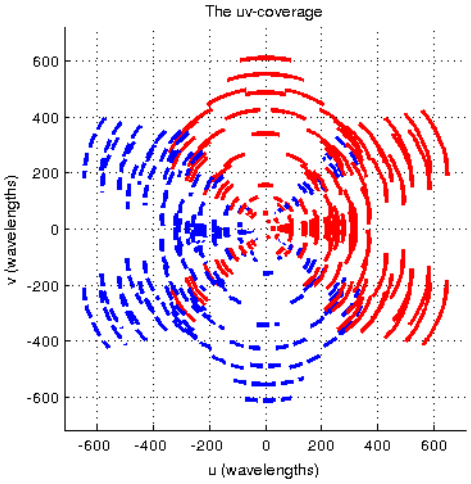

Figure 3.12: The uv-coverage for 45° declinations for a 2 hour observation

tions are given in Equation (3.7.1) [6][45].

$$W(u,v) = \sum_{k=1}^{N} T_k Q_k \delta(u-u_k, v-v_k). \tag{3.7.1}$$

Here N represents the number of the uv elements, T_k represents the tapering effects and Q_k is the density weights and $\delta(u-u_k, v-v_k)$ is the 2-dimensional delta function. If the sampling function S, also known as the uv-coverage had no gaps, then the PSF B would not have side lobes. However, in practice the sampling function is given by a linear combination of delta functions, with the interferometer spacings corresponding to the points in the uv-plane [47; 48].

The finite projected baseline corresponding to two antenna elements provides a finite limit to the extent of the uv-plane. In practical instances more data

Stellenbosch University https://scholar.sun.ac.za

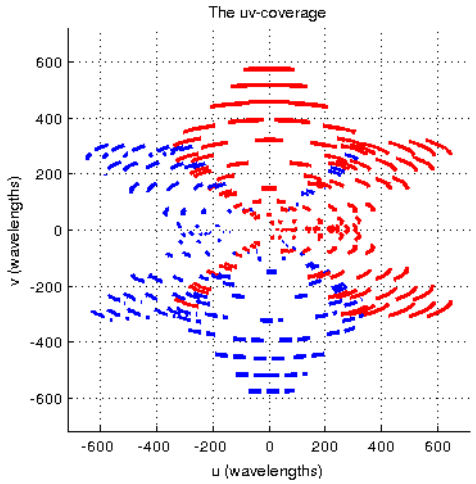

Figure 3.13: The uv-coverage of a snapshot at 45° declination

falls within the inner region of the uv-plane than further out, which then tends to give higher weights to the low spatial frequencies (i.e the data that is more dense at the center). The variable σ^2 in Equation (3.7.2) adjusts the width of the gaussian taper.

$$\mathbf{T_k}(u,v) = e^{-(u^2+v^2)}/\sigma^2 \tag{3.7.2}$$

This kind of uv-sampling tends to impair the deconvolution of I. These practical real life problems make it impossible for the astronomers to obtain their desired beam (which is without side lobes). The weighting functions Q_k and T_k are arbitrary. They can be specified to fine-tune the beam shape and prevent the natural sampling as much as possible [49].

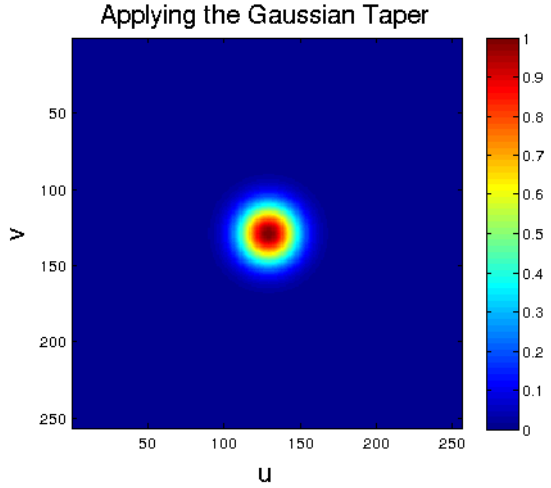

Figure 3.14: The Tapering weighting function

Stellenbosch University https://scholar.sun.ac.za

The tapering weights T_k 3.7.2 [45] are used for down-weighting data at the outer edge of the uv-coverage, and thus to suppress small-scale side lobes. The density weights Q_k are used to offset the high concentration of (u,v) tracks near the center and to lessen the side lobes caused by gaps in the coverage.

The density function Q_k can be used for compensation of the clumping of data in the uv-plane by weighting the reciprocal of the local data density. Natural weighting, with all points treated alike, gives the best signal-to-noise ratio for weak source detection. However, since the uv-tracks tend to be more clumped near the (u,v) origin, natural weighting emphasises the data from the short spacings and tends to produce a beam with a broad, low-level plateau. This latter is undesirable when imaging sources with both large and small scale structure [7].

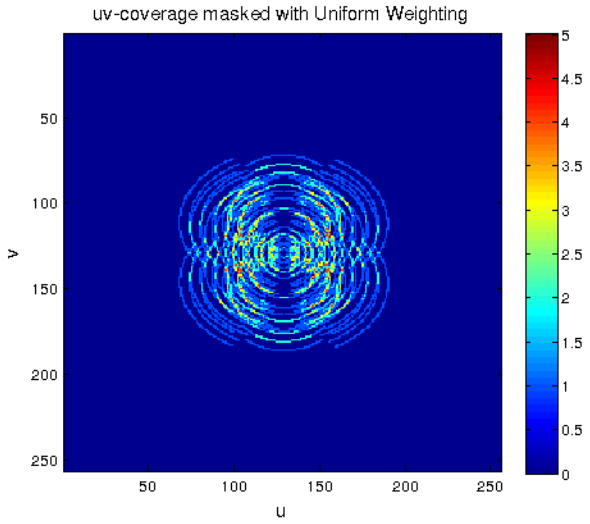

Figure 3.15: The Uniform weighting

Uniform weighting commonly counts all the points that lie within a rectangular block of grid cells in the neighborhood of the k^{th} datum. This produces a beam shape specified largely by the tapering function T_k.

Stellenbosch University https://scholar.sun.ac.za

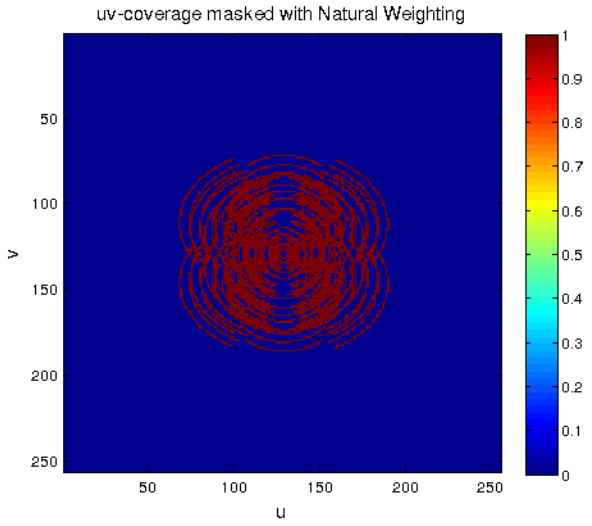

Figure 3.16: The Natural weighting

3.7.1 Gridding the Visibility Data

To take advantage of the extremely efficient FFT algorithm, visibility values must be assigned to a regularly, rectangular matrix or "grid", usually with a power-of-two number of points each side, since the observed data does not normally lie on such a grid. Some procedure must be used to assign visibility values at the grid points based on the observed values. A method called gridding can be used to regularise the irregularly sampled data.

The array configurations and baseline lengths provides us with a finite space onto which we want to transform our data. A space that is finite can also be thought of as an infinite space multiplied by a truncated windowing function. For this work the visibilities and the sky model were arranged onto a uniform rectangular grid, where each pixel of the intensity map, corresponds to a pixel in the visibility function.

The gridding procedure is often approximated by a convolution, where the irregularly spaced data is convolved with a gridding convolution kernel, where the gridding convolution kernel is the FT of the window function. Convolution is not a pure interpolation procedure, since it combines smoothing or averaging with interpolation. The resulting convolved data is sampled at regular intervals and finally the FFT can be used for the data transformation [6; 25].

3.8 Conclusion

This chapter has reviewed the literature for interferometry and imaging. The chapter began with a motivation for the use of interferometry instead of single

Stellenbosch University https://scholar.sun.ac.za

antennas and goes on to explain a 2-element interferometer. The underlying principles of interferometry and imaging that are necessary for the understanding of this work have been fully discussed.

Simulations illustrating earth rotation aperture synthesis, coordinate systems, visibility function, intensity distribution function and uv-coverage have been fully discussed. The relationship between the uv-sampling and the uv-coverage has been discussed and the weighting functions have also been explained and graphically illustrated. These concepts have been explained and illustrated using simulations of antenna configurations like the VLA.

This chapter is critically important as it lays the imaging foundation needed throughout this work. The chapter(s) on deconvolution and A-Stacking that follow, build on the concepts discussed in this chapter.

Stellenbosch University https://scholar.sun.ac.za

Chapter 4

Deconvolution and the CLEAN algorithm

4.1 Introduction

In this chapter we briefly describe deconvolution, the dirty map, dirty beam and then in detail, the *Högbom* CLEAN algorithm. There exists a number of variations of this algorithm, which we will not discuss in detail in this work, but mention them nonetheless. Generally, the process of deconvolution means separating or deconvolving terms that are combined together by a convolution.

Imaging usually refers to the process of transforming visibilities in the spatial frequency domain to the approximate sky representation in the spatial domain and deconvolving the array PSF from the dirty image in an attempt to recover the true sky. The CLEAN algorithm is fully examined and implemented in this chapter.

4.2 Deconvolution

The method of Aperture Synthesis is designed to produce high quality images of sources by combining a number of measurements for different antenna spacings and orientations [29]. In radio interferometry, the large separations between telescopes implies high resolution and the interferometer measures visibility measurements at irregular samples. The irregularly sampled uv-coverage is then Fourier transformed to give the PSF.

The process of transforming the uv-coverage can be efficiently computed using the fast FFT, which requires that the data be regularly sampled. The theory of aperture synthesis does not require that the uv-plane must be covered with regular distribution of baseline measurements [45; 46]. However, a regular distribu-

Stellenbosch University https://scholar.sun.ac.za

tion will generally produce maps which are relatively easy to analyze. It is impractical for high-resolution radio interferometry to arrange the measured baselines into a regular distribution.

The resulting gaps in the uv-plane give rise to sidelobes in the synthesised beam and make it complicated to analyze the dirty map. Irregularities in the baseline coverage can also be because of the occultations of radio signals by the moon [1], interference and some malfunctioning of the equipment since data corrupted by RFI will be flagged [6]. Deconvolution is to correct for the dirty map artifacts due to the gaps in the uv-plane and the clean map is iteratively deconvolved from the dirty map and the known dirty beam by CLEAN.

Deconvolution initially appears to be a fairly trivial operation at first glance since we know how to convolve two functions and produce a new function. Let us consider deconvolution anal,tically. Consider two arbitrary functions f and g resulting in a new function h.

$$h = f * g \tag{4.2.1}$$

So, given f and g the convolution theorem gives (4.2.1) where h is the resulting new function. Taking the FT of the above equation, we obtain (4.2.2).

$$\begin{aligned} \mathscr{F}\{h\} &= \mathscr{F}\{f * g\} \\ &= \mathscr{F}\{f\}\mathscr{F}\{g\} \end{aligned} \tag{4.2.2}$$

The resulting FT of the functions f and g are given by F and G. The process of deconvolving F is illustrated in (4.2.3).

$$\begin{aligned} H &= FG \\ F &= \frac{H}{G} \\ \mathscr{F}^{-1}\{F\} &= \mathscr{F}^{-1}\{\frac{H}{G}\} \end{aligned} \tag{4.2.3}$$

We see that F and thus f can be deconvolved analytically if G is not zero. For our case, the transfer function contains areas where it is zero. This is due to the fundamental problem where some visibilities are not measured. This indicates that any procedure that aims to improve the intensity derived using other methods other than weighting the visibility must therefore place non-zero visibility values at the unmeasured visibility (uv) areas [41].

In 1954 it was pointed out by Bracewell and Roberts that there exists an infinite number of solutions for the convolution in equation (4.2.1) since one can add arbitrary visibility values in the unsampled areas of the uv-plane [24]. However,

[1] This is the case where the moon is positioned between the earth and the desired point of interest.

Stellenbosch University https://scholar.sun.ac.za

the FT of these added values constitutes a distribution that can not be detected by any instrument with corresponding zero areas in the transfer function.

It remains arguable that in interpreting the observations from radio telescopes, one should maintain only zeros in the areas of unmeasured visibilities to avoid arbitrarily generating information. On the other hand the zeros themselves are arbitrary values, some of which are certainly wrong. What is desired is a procedure that will allow the visibilities at the unmeasured points in the uv-plane to take consistent values with the most reasonable or likely intensity distribution, while minimizing and possibly eliminating the addition of arbitrary details. Which therefore introduces the CLEAN algorithm originating from the $Högbom$ CLEAN and later variations of the algorithm [25; 50; 7].

4.2.1 The Dirty Map and the Dirty Beam

Considering the $Van\ Cittert-Zernike$ theorem which states that under certain conditions the FT of the mutual coherence function for an incoherent, distant source equals to its complex visibility. The relationship between the visibility function $V(u,v)$ and the sky brightness $I(l,m)$ is given by the following equation [19; 51; 50].

$$\begin{aligned} I(l,m) &= \int_{-\infty}^{+\infty}\int_{-\infty}^{+\infty} V(u,v)e^{2\pi i(lu+mv)}\,du\,dv, \\ &= \mathscr{F}^{-1}[V(u,v)]. \end{aligned} \tag{4.2.4}$$

Consider the existence of the Fourier relationship between the visibility data $V(u,v)$, true sky brightness distribution $I(l,m)$. Practical interferometers measure discrete baseline measurements in the uv-plane, which is analogous to sampling the uv-plane. These sampled visibility measurements are also referred as the uv-coverage [52]. In using Fourier analysis, taking the inverse FT of the uv-coverage gives the synthesized or dirty beam, say $b^{'}(l,m)$, where $b^{'}(l,m)$ will have distortions and undesirable side lobes because of the gaps in the uv-coverage. However, from convolution theory, a convolution in one domain is equal to a multiplication in the other domain [53; 54].

Clearly, if the uv-coverage had no gaps and extended to infinity, then the dirty beam would have the appearance of a delta function. This result is a direct implication that the true brightness distribution $I(l,m)$ is the same as the dirty map $I^D(l,m)$. However, this case is purely ideal and impractical because unavoidable physical limitations cannot produce a complete uv-coverage, i.e antenna configurations [45; 25]. A synthesized beam (dirty beam) is also known as a point spread function (PSF) which is the measure of how a single point source due to

Stellenbosch University https://scholar.sun.ac.za

under sampling is smeared or spread.

The dirty map is the convolution of the sky brightness distribution $I(l,m)$ with the PSF. The CLEAN algorithm is designed to approximate a more accurate visibility data $V(u,v)$ by removing the effects of the synthesized beam [55; 56]. One may wonder why is the deconvolution performed iteratively with CLEAN instead of a direct analytical mathematical approach. It is performed iteratively because the uv-coverage and the PSF are not invertible, they contain zero values (as already discussed). The dirty image is denoted by equation (4.2.5).

$$\begin{aligned} I^{'}(l,m) &= \int_{-\infty}^{+\infty}\int_{-\infty}^{+\infty} S(u,v)V(u,v)e^{2\pi i(lu+mv)}\,du\,dv, \\ &= \mathscr{F}^{-1}[S(u,v)V(u,v)], \end{aligned} \tag{4.2.5}$$

where V is the observed visibility and S is the sampling function. From the convolution theory, $*$ denotes a convolution as stated above and thus we have equation (4.2.1).

$$\mathscr{F}[f*g] = \mathscr{F}[f]\mathscr{F}[g] \tag{4.2.6}$$

Therefore $I = \mathscr{F}^{-1}[V]$ is the clean map and therefore the images below are that of a randomly generated sky and the dirty image generated from it. The figure 4.1 below has been simulated on a 512×512 size image. The 5 point sources are randomly generated and have varying magnitudes between 0-1 jy and are all generated more than 20 pixels from the edge of the image. The red rings around the sources are used to highlight the sources and the axis are in pixels. The observation will be a 6 hour observation (hour angle ranging from -3h to 3h) integrated every 300 seconds.

Stellenbosch University https://scholar.sun.ac.za

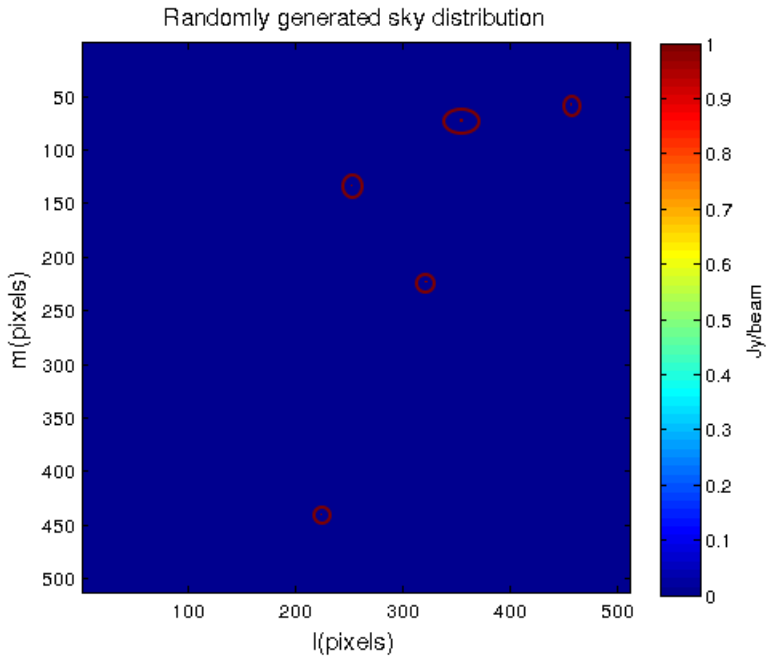

Figure 4.1: An image of a randomly generated sky $I(l,m)$.

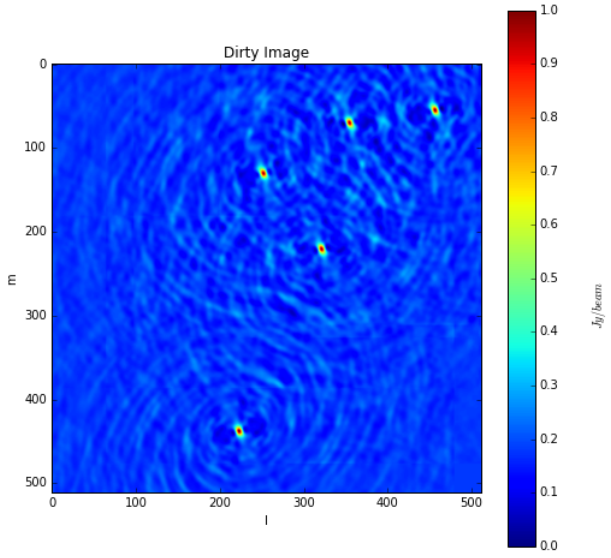

Figure 4.2: The corresponding computed dirty image $I^{'}(l,m)$.

However, to be able to compute the dirty map we need to define the dirty beam, which is defined as the inverse FT of the uv-coverage. The PSF that was used to obtain Figure 4.2 is shown in Figure 4.3. A VLA-like antenna configuration

Stellenbosch University https://scholar.sun.ac.za

was simulated with 11 antennas. The observers latitude was taken at 35° and the source declination taken to be 45° over a 6 hour observation. The dirty beam is independent of the sky; it depends on parameters such as the array configuration, declination and hour angle of observation and time of the observation etc [42]. Observing for an extended amount of time, with strategically arranged antennas in an array allows for the uv plane to be sampled better due to earth rotation, which increases sensitivity. The dirty beam $b^{'}$ is computed as:

$$b^{'} = \mathscr{F}^{-1}[S]. \tag{4.2.7}$$

Finally, the dirty map is given by:

$$I^{'} = \mathscr{F}^{-1}[S(u,v)V(u,v)], \tag{4.2.8}$$
$$= \mathscr{F}^{-1}[S(u,v)] * \mathscr{F}^{-1}[V(u,v)], \tag{4.2.9}$$
$$= I * b^{'}. \tag{4.2.10}$$

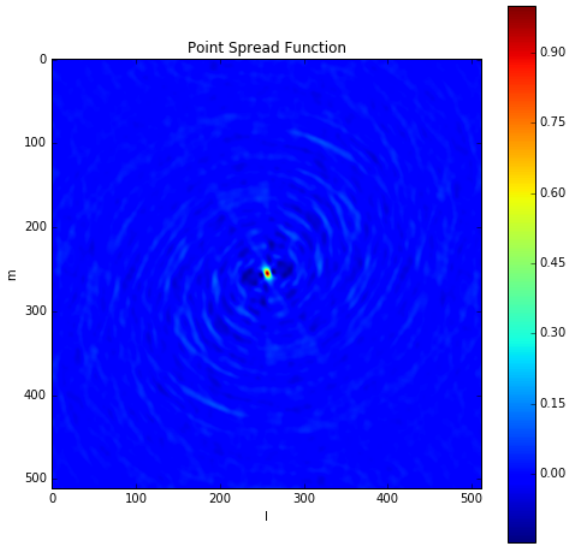

Figure 4.3: The PSF using a VLA-like array configuration.

From the above images and discussion we note that a better PSF can be obtained by varying the parameters such as the frequency bandwidth and time. The uv-coverage is a function of declination, array configuration and time [43; 45].

Stellenbosch University https://scholar.sun.ac.za

4.3 The CLEAN Algorithm

The CLEAN algorithm is an iterative procedure that was developed by *Högbom* in the 1970's. CLEAN uses the known shape of the dirty beam and operates in the image domain to distinguish between real structure and side lobe artifacts in the dirty map. It produces a more accurate true sky distribution model [6; 46]. To compute the algorithm, we need to have the following. The algorithm is summarised in Figure 4.4 and was implemented in Matlab.

Stellenbosch University https://scholar.sun.ac.za

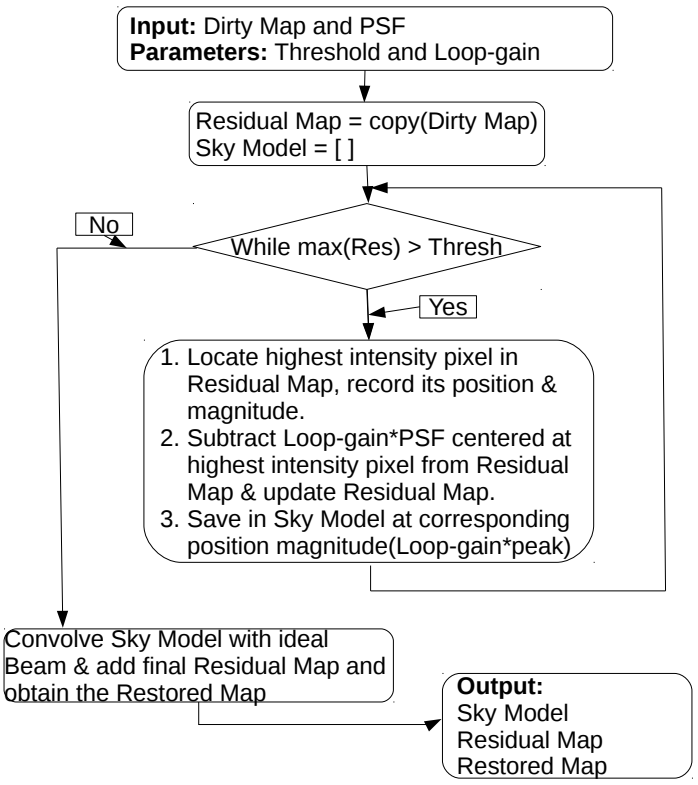

Figure 4.4: Pseudocode for the *Högbom* Clean algorithm as implemented in this chapter.

In the above Figure 4.4, Loop-gain*PSF represents the multiplication of the loop gain with the PSF. The "Sky Model = []" is an empty bin that is appended at each iteration until the condition is met.

The iterative procedure for the CLEAN algorithm is as follows:

1. We start by making a copy of the dirty map ($I^{'}$)and rename it as the residual map $I^{'}_{res}$.

Stellenbosch University https://scholar.sun.ac.za

2. Search for the strongest intensity pixel in the residual map, record its position and magnitude max($|I'_{res}|$).

3. Create a model of the same size as the sky distribution I and place γ.max($|I_{res}|$) at its spatial position to the model.

4. Subtract from the residual map the PSF multiplied by the loop gain and amplitude of the peak at the position of the peak.

5. Repeat the process from 2 again until the threshold has been reached where the threshold has been defined to be 10 percent of the peak residual. Initially the peak residual is the magnitude of the highest peak in the dirty map, then 10 percent of that value is the threshold. The threshold remains constant, but the peak is gradually changing with each subtraction.

6. Convolve the resulting model by a restoring CLEAN beam which is usually a fitted Gaussian because of its desired sidelobe level.

7. Add the final residual map to the clean image to form the restored image.

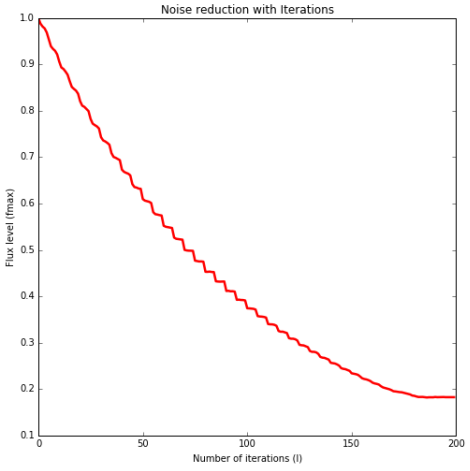

Figure 4.5: The relationship between number of iterations and residual flux during the iterative CLEANing procedure.

Stellenbosch University https://scholar.sun.ac.za

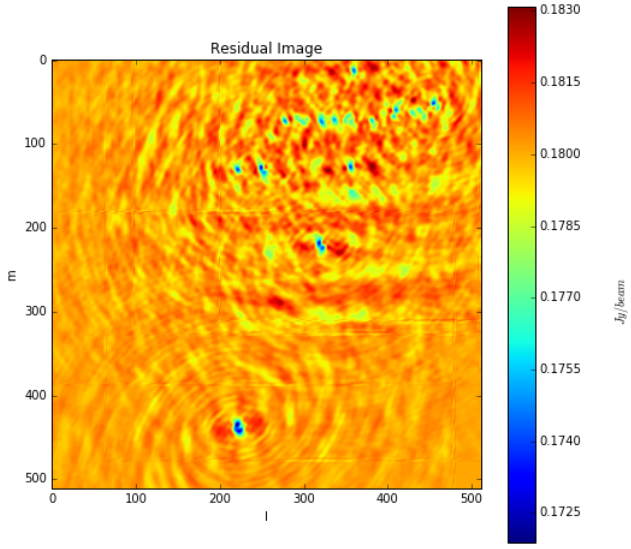

Figure 4.6: Residual image as obtained at the end of the iterative subtraction by CLEAN.

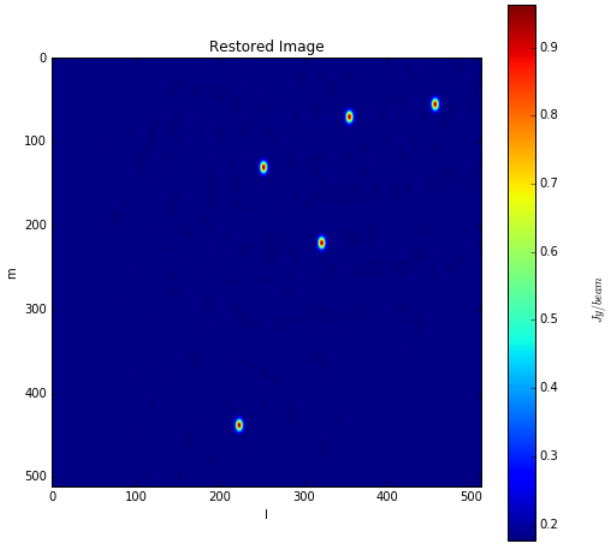

Figure 4.7: The restored image after the CLEANing procedure.

Stellenbosch University https://scholar.sun.ac.za

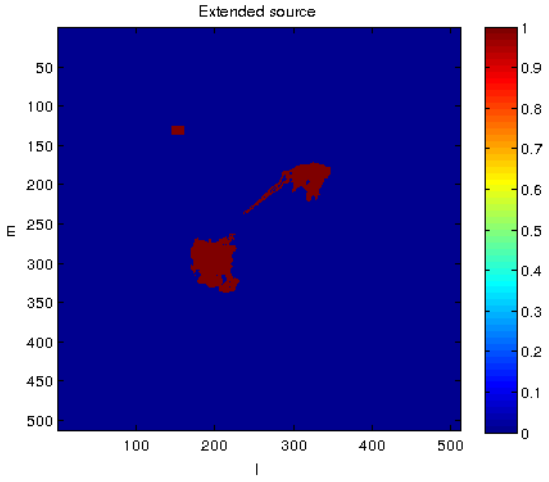

Figure 4.8: A random Extended source created using Matlab.

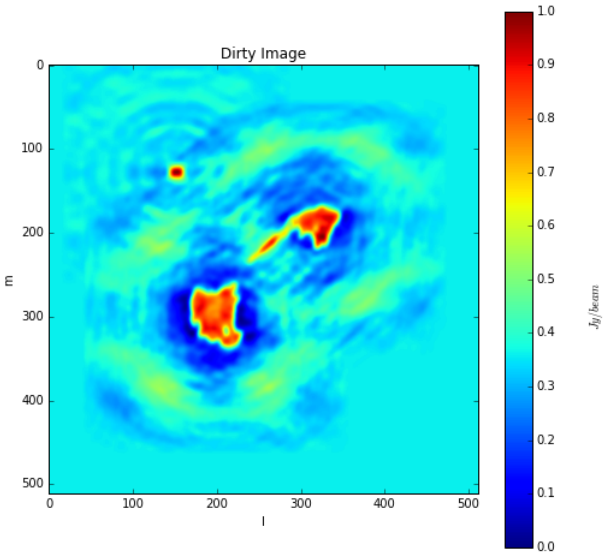

Figure 4.9: Dirty image of the extended source.

Stellenbosch University https://scholar.sun.ac.za

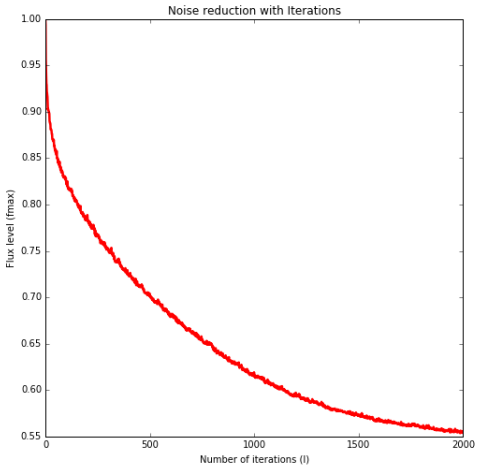

Figure 4.10: Intensity magnitude vs Number of iterations.

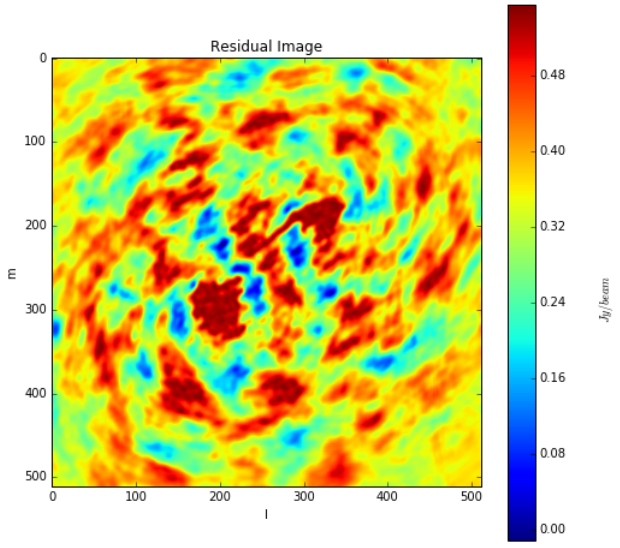

Figure 4.11: Extended source residual image.

Stellenbosch University https://scholar.sun.ac.za

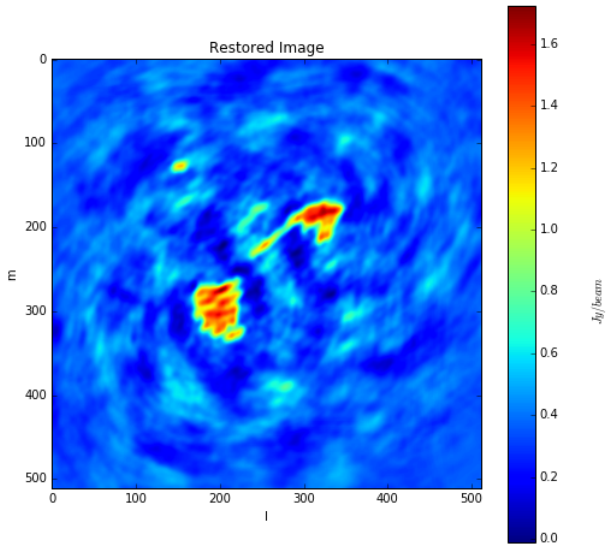

Figure 4.12: Extended source restored image.

From the simulated Figures 4.5 to 4.12 we note that CLEAN is not perfect and that the results depend on the above defined parameters. The scale factor γ is called the loop-gain and it determines the convergence of CLEAN. The loop-gain is to be chosen to be $0 < \gamma < 1$ in theory. However, in practice the loop-gain should be $\gamma \simeq 0.1 - 0.2$, depending on the side lobe level and source structure [6]. Therefore in principle, higher values of γ result in faster convergence of the method and hence the loop gain is chosen to be small so that smaller "peels" of the identified structures are iteratively subtracted. This is shown in Figures 4.5 and 4.10 where for the same loop gain, clean converges at different values of flux magnitude. Flux magnitude is computed in every iteration since the magnitude of the residual map is decreasing, it is the highest peak in every iteration. As shown in Figure 4.10 that even though more subtractions have been computed in comparison to Figure 4.5, the convergence point is still higher for the extended source. This is because CLEAN treats an extended source as a sum of point sources and then starts to subtract an extended source like a field of point sources. Hence, more iterations and yet higher convergence for the extended source when the loop gain is made to be the same.

The residual map is the map derived from the dirty map; it is the map where the iterative point source subtraction takes place. When all sources have been subtracted, ideally it is expected that only base level noise should be remaining as the residual map [25]. The sky model and the residual map are expected to behave inversely proportional during the iterative process. As the sky model is be-

Stellenbosch University https://scholar.sun.ac.za

ing filled by identified and subtracted sources from the residual map, the residual map is supposed to be descending to noise as source structure is being iteratively removed.

The recovered sky image, is the image where the sky model is convolved with the CLEAN beam, which is a Gaussian scaled according to the differently sized subtracted sources and added to the final residual map [6; 46]. The recovered sky is therefore an approximation of the true sky which is obtained from the dirty map through deconvolution.

A threshold acts like a limit for the Clean algorithm, The algorithm iterates until it reaches 10 percent of the peak flux in the dirty map. Usually the threshold is about 10 - 25 percent of the peak flux, just above the noise level. Also, iterations in this case represent the number of subtractions and depend on the defined threshold and loop-gain. If the loop-gain is relatively low, then the number of iterations will increase. It is noted that noise can not be completely eliminated from practical systems, although it can be minimised extensively.

Noise makes it difficult for the deconvolution algorithms to locate and subtract weak sources as they are easily contaminated and therefore knowledge of the sky is important through verification using image catalogues [45]. It would be ideal to remain with the base levelnoise after the CLEANing has been done, which depends on the stopping criteria. If the stopping criteria is not properly defined, weak sources might not be recovered after CLEANing as they would have been masked by noise and CLEANing stopped before recovering them. On the other hand, if the threshold is too low then the image might be over CLEANed, where over CLEANing would be a case where even noise peaks might be CLEANed and identified as sources by the algorithm [46].

We have illustrated using figure 4.5 that the residual flux in the residual image decreases with increasing number of subtraction until a noise level is reached. The final residual map has been shown in figure 4.6 and similarly the recovered or restored image in 4.7. For these simulation results it is important to note that the threshold has been set at 10 percent for both point-like and extended sources. Also, the number of iterations for the extended source is 2000 at flux level of about 0.55 in comparison to point-like sources converging with only 200 iterations at about 0.9 the flux level. This means a large number of iterations for an extended structure is required to achieve equivalent flux level of a point source like structure. This is because CLEAN treats an extended structure as a summation of point sources.

Stellenbosch University https://scholar.sun.ac.za

4.4 CLEAN Variations

The *Högbom* CLEAN has a number of variations which are conceptually the same as the original CLEAN algorithm, but are more efficient. The Clark CLEAN algorithm is one of such algorithms, It introduces the concept of minor and major cycles. It makes use of the insight that since the repeated shift, scale and addition iterations performed in the *Högbom* Clean are essentially a convolution of the clean components with the dirty beam; the procedure may actually be improved by the use of the FFT. The minor cyle proceeds more like the *Högbom* Clean, except that the considered residuals are those of intensities larger than α times the peak residual; where α is a fraction of the largest sidelobe [25].

The processing format is list based and considering a beam patch [2] limits the interaction between pixels. This results in an approximation of the CLEAN components which would have been computed by *Högbom* Clean, but one which can be quickly computed compared to *Högbom* Clean. The algorithm enters the major cycle when the approximation starts to break down [3] and via a single FFT pair, the algorithm computes the residuals of the clean component model accumulated. The model is then transformed into the visibility domain and multiplied by the uv-coverage (the weighted sampling function which is the FT of the PSF). It is then transformed back into the image domain and differenced with the original dirty map. This allows errors introduced by the approximation to be corrected [7]. The Clark CLEAN is ideal for parallelism since the dirty mat is divided into windows which can be cleaned separately.

The other variant of the *Högbom* Clean is the Cotton-Schwab algorithm. This algorithm also uses minor and major cycles. The only difference is in the major cycle, that the model components are not subtracted from the dirty image; but from the visibility data and therefore aliasing due to the convolutional gridding is nearly eliminated [7].

This method allows for multiple fields to be imaged simultaneously. These multiple imaged fields then undergo the minor cycle and independently. The distant sidelobes are removed during the major cycle from other fields. The Cotton-Schwab Clean is the algorithm of choice when considering many real-world imaging problems because when the residuals are computed, the w term is properly considered for each subfield [45]. The multi-scale CLEAN is another variation of the *Högbom* CLEAN algorithm

[2] This chosen area is only a region of the beam near the center centered at the beam center.

[3] The approximation breakdown is when the peaks are over subtracted such that the residual is cleaned deep enough.

Stellenbosch University https://scholar.sun.ac.za

4.5 Conclusion

In this chapter, Deconvolution and the *Högbom* CLEAN algorithm in particular have been fully discussed. Other deconvolution algorithms have been briefly mentioned. The *Högbom* CLEAN has been implemented, making use of the randomly simulated sky and the resulting synthesized dirty beam and dirty maps.

It has been shown that the algorithm works well for point-like structures and not so well with extended structure as it recognizes an extended structure to be a collection of point sources. The variants of CLEAN which were not implemented in this work are better equipped to handle such cases. The sky models in this section were simulated using Matlab; the dirty beam used for both cases (point source and extended source) was obtained using the VLA-like antenna configuration. The loop gain for both cases was made to be 0.05 to allow small scales to be peeled at a time. As expected the CLEAN algorithm performed well for the point sources and not so good with the extended source.

Stellenbosch University https://scholar.sun.ac.za

Chapter 5

The A-Stacking Algorithm

5.1 Introduction

In this chapter the A-Stacking algorithm will be implemented and Direction-Dependent and Baseline-Dependent effects will be examined. The literature will be fully reviewed showing images and graphs to give a full explanation of the subject. The simulations using FEKO of the LOFAR-like and PAPER-like antenna arrays will be computed to show the beam pattern distortions due to mutual coupling which has been accounted for. At low frequencies, the array elements happen to be in each others NF and then couple with each other; resulting in the antenna gain matrix being a function of both baseline and direction. Due to this, the FT relashionship breaks down and the A-Stacking algorithm suggests a parametric linear model to solve this problem.

5.2 A-Stacking

The failure to correct for Direction-Dependent (DD) effects like the antenna radiation patterns, non-coplanar baselines, antenna pointing errors, effects of spherical geometry for widefield imaging such as the w-term and ionospheric phase delays would result in a limited imaging performance. However, knowing the DD effects does not imply they will be efficiently corrected for. These effects vary with time and are different for different antennas in an interferometer array.

The variation of these effects with antenna elements does not only make them directional-dependent, but also baseline-dependent (BD) which results in a breakdown in the Fourier relationship between the visibilities and the intensity distribution [3]. The beam patterns tend to show variability or distortions due to mutual coupling, which are different depending on directions of elements. Since in this study we do not intend to simulate the LOFAR and PAPER arrays, but LOFAR-like and PAPER-like arrays and also want to show the computational complexity trade-off. The arrays in this Chapter are randomly distributed and simulated us-

Stellenbosch University https://scholar.sun.ac.za

ing FEKO, but now the antennas have been randomly increased to 35 so as to clearly illustrate the decrease in relative error over a reasonable number of terms. These arrays result in 560 baselines; FEKO was run over a range of frequencies (10 to 80 MHz in steps of 5 MHz). Only one polarization was used as the antennas were excited at the bottom port as explained earlier.The ionosphere varies across the field of view due to varying density of the Total Electron Content (TEC) and the different elements have different beam shapes because $A(l,m)$ is different for each baseline, hence baseline-dependent.

Consider a case where an array of antennas would be observing a source at an arbitrary declination, say 50°. Differnt baselines will have different $A(l,m)$ due to phase delays and other ionospheric disturbances. Also since mutual coupling is not just dependent on the distance between the antennas, but also their orientated they are relative to each other. For example, an antenna located at $(0,0)$ might couple with an antenna at distance x away from it along the same axis and also if that same antenna is at the same distance, but at an oblique angle relative the reference antenna; the degree of coupling will be different. For this we acknowledge the fact that the non-identical primary beams of antenna elements in arrays are due to a number of factors, but for this work we will focus on the effects of mutual coupling. Thorough discussion of the signal path and expected distortions as the signal passes through the ionosphere are discussed in Appendix A.

Considering a practical case where the ionosphere is varying across the FoV, the perceived sky will be different for different directions. The direction-dependence means that the primary beam patterns will be different at different directions. Baseline-dependence means that having picked a reference antenna, varying baseline lengths and orientations will also result in different antenna patterns.

5.2.1 The Interferometer Response

The response of an interferometer as already discussed in chapter 2 is given by the equation 5.2.1, which can also be compactly denoted by equation 5.2.2.

$$V(u,v) = \iint I(l,m)e^{-2i\pi(ul+vm)}dldm \tag{5.2.1}$$

$$\mathbf{v} = \Phi\sigma \tag{5.2.2}$$

Here $\mathbf{v}$ is a vector of $K \times 1$ complex valued visibilities that have been measured by the array; σ is a $N_p^2 \times 1$ vector where each element represents a pixel intensity from an $N_p \times N_p$ model of the sky and ϕ is a matrix representation of the Fourier transform, inwhich the element in the k^{th} row and n^{th} column equals to Equation 5.2.3. Equation 5.2.2 is a discretized version of Equation 5.2.1. [3]

Stellenbosch University https://scholar.sun.ac.za

$$\phi_k^{(n)} = e^{-2i\pi(u_k l_n + v_k m_n)}, \tag{5.2.3}$$

where k denotes the baseline index, n is the pixel index and (u, v) and (l, m) are as discussed in Chapter 2.

The inverse Fourier transform of 5.2.1 and 5.2.2 may be performed in order to obtain the image of the sky. However, the inversion is mostly computed iteratively and the efficiency of the FFT is desirable. The FT in 5.2.2 can then be computed with the FFT and then followed by the degridding step.

This is due to the fact that a practical interferometer does not sample the visibility regularly as is required by the FFT. Therefore, a gridding step in the form of convolution is required to relate the visibilities on the FFT grid to those at the antenna array sampling positions.

If we then include the direction-dependent baseline-dependent antenna gain patterns into Equation 5.2.2, the Fourier relationship breaks down. Consider Equation 5.2.4 where $A_k(l, m)$ represents the antenna gain patterns [3]. We note the subscript k implies that for different baselines the interferometer measures a different visibility function. This is clearly shown by equation 5.2.5 where we assume a hypothetical array for which $A_k = 1$. In this particular case, for all baselines the hypothetical array would "see" the same perceived sky.

$$V_k(u, v) = \iint A_k(l, m) I(l, m) e^{-2i\pi(ul+vm)} dl dm. \tag{5.2.4}$$

Assuming a hypothetical interferometer measures visibilities V_0, where $A_k = 1$.

$$\therefore V_0(u, v) = \iint I(l, m) e^{-2i\pi(ul+vm)} dl dm. \text{[3]} \tag{5.2.5}$$

The A-Stacking algorithm aims to correct this problem by separating the direction and baseline dependence through the use of an appropriately defined linear model. In this algorithm, the image to visibility calculation allows a fast computation of the repeated FFTs as it assumes a form of a combination of separate FTs.

The number of terms in the model determines the accuracy of the calculation and therefore gives a trade-off between the computational cost and the accuracy. The singular value decomposition method is used to sufficiently and efficiently describe these effects accurately, results then show that the method is most efficient when described by relatively few terms [3].

Stellenbosch University https://scholar.sun.ac.za

5.3 The A-Stacking formulation

Assume that $A_k(l,m)$ can be written as a linear model in the following form of N_B basis functions.

$$A_k(l,m) = \sum_{i=1}^{N_B} a^{(i,k)} f_i(l,m), \tag{5.3.1}$$

where $a^{(i,k)}$ are the expansion coefficients corresponding to a specific baseline k while the $f_i(l,m)$ denotes the DD basis function common to all baselines. Using the discrete form of equation 5.2.4, we have the following.

$$\mathbf{v} = (\Phi \odot \mathbf{B})\sigma, \tag{5.3.2}$$

here $\odot$ is the Hadamard product and $\mathbf{B}$ is the multiplicative distortion matrix where,

$$\mathbf{B} = [\mathbf{b}_1 \mathbf{b}_2 \dots \mathbf{b}_k]^T \tag{5.3.3}$$

$$\Phi = \left[\phi_1 \phi_2 \dots \phi_k\right]^T \tag{5.3.4}$$

where each $\mathbf{b}_k$ is a $N_P^2 \times 1$ complex valued vector discretization of the radiation patterns over the image plane [3]. The form of equation 5.3.2 does not allow for the use of the FFT. In denoting the $N_P^2 \times 1$ vector discretization of f_i in the image plane by $\mathbf{f}_i$, equation 5.3.1 is given by,

$$\mathbf{b}_k = \sum_{i=1}^{N_B} a^{(i,k)} \mathbf{f}_i, \tag{5.3.5}$$

where the baseline dependence is accounted for by the coefficients $a^{(i,k)}$ and the basis function $\mathbf{f}_i$ accounts for the direction independence. Substituting this expression into equation 5.3.2 gives,

$$\mathbf{v} = \sum_{i=1}^{N_B} \text{diag}(\mathbf{a}_i)\boldsymbol{\Phi}\text{diag}(\mathbf{f}_i)\boldsymbol{\sigma}, \tag{5.3.6}$$

and we have $\mathbf{a}_i = \left[\mathbf{a}^{(i,1)} \mathbf{a}^{(i,2)} \dots \mathbf{a}^{(i,k)}\right]^T$.

5.3.1 A-Stacking: Forward calculation

The forward calculation of A-Stacking takes the sky model and transform it into the visibilities. This is now the desired form relating the visibilities to the discretized sky, while fully accounting for the BD-DD effects the visibilities can be computed as follows:

Stellenbosch University https://scholar.sun.ac.za

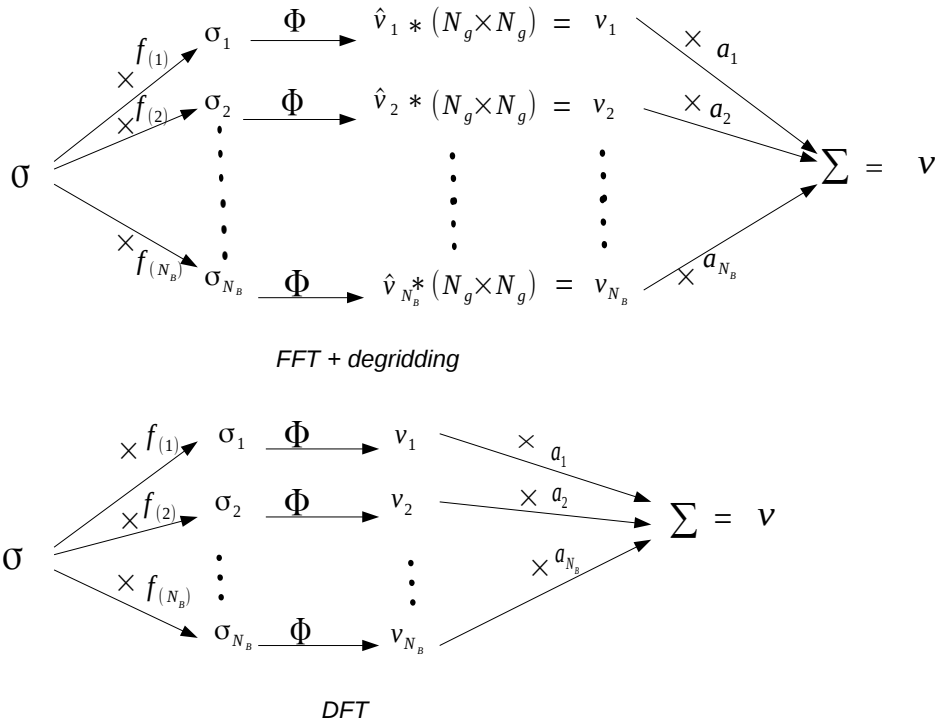

Figure 5.1: Schematic representation of the A-Stacking algorithm; first part illustrating the use of the FFT + degridding and the second part highlighting the computation using the DFT.

1. The image domain correction is applied in the form of element-wise multiplication to compute the apparent skies and a matrix of diagonal basis functions multiplies the true sky (per-basis function).

$$\boldsymbol{\sigma_i} = \text{diag}(\mathbf{f}_i)\boldsymbol{\sigma} \tag{5.3.7}$$

2. Taking the Fourier transform of each apparent sky gives a corresponding set of visibilities. This is computed efficiently using the FFT and followed by degridding.

$$\mathbf{v}_i = \boldsymbol{\Phi}\boldsymbol{\sigma_i} \tag{5.3.8}$$

3. A correction in the visibility domain is applied in the form of element-wise multiplication to each visibility and summing the result.

$$\mathbf{v} = \sum_i^{N_B} \text{diag}(\boldsymbol{a}_i)\mathbf{v}_i \tag{5.3.9}$$

The quantities σ_i and $\mathbf{v}_i$ are dependent and can be computed serially, but calculation from σ_i to $\mathbf{v}_i$ can be computed parallel for different i values because $\mathbf{v}_i$

Stellenbosch University https://scholar.sun.ac.za

depends on a single σ_i. The overall computational cost of the above procedure is given by,

$$\mathcal{O}(N_B(N_p^2 + N_p^2 \log N_p) + N_B K N_g^2) \tag{5.3.10}$$

where the first term accounts for the per-basis function correction in the image plane and the FFT, the last term accounts for the gridding and the correction in the visibility plain; that is, $N_g \times N_g$ is the size of the gridding kernel. The computational cost increases with the number of basis functions. Due to the computational complexity scaling linearly with basis functions, it then becomes desirable to choose a suitable basis. A basis is generally defined as a linearly independent generating set, so this will allow high accuracy for a small number of terms. This basis is then computed using the singular value decomposition method.

The Figure 6.6 clearly illustrates that accuracy of the forward calculation and we note the trade-off between number of terms and the relative error. The relative error is computed by obtaining the difference between the exact visibilities and the model visibilities. When computing the forward calculation, the second part of figure 5.1 was used and not the FFT + degridding. The Figure 5.1 is to show two options of computing the visibilities, using the FFT + deggriding method or using a DFT method, where gridding/degridding is not performed. This is because the FFT requires and additional gridding/degridding step for irregularly spaced data, unlike the DFT.
For the above results illustrating the simple trade-off between the computational efficiency and the accuracy in the calculation of the forward calculation; a LOFAR-like (LBA) array was simulated at a wide frequency band of around (10-80)MHz, using a single polarization. As it has been discussed that the distribution of the LOFAR-like elements is random and some antennas are in close proximity. The simulation of these elements was computed in FEKO and radiation patterns analysed, taking into consideration the mutual coupling effects. A 16×16 image grid was used to simulate a model sky with 5 point source-like structures of varying intensities using Matlab. The array configuration is random, computed in Matlab and fed into FEKO and this is a snap-shot observation.

The simulated sky model was then used as input in computing the measured visibilities using equation 5.3.2. Different approaches have been used to calculate model visibilities, such as (1.) using equation 5.3.2 and averaging the power patterns over all antennas and (2.) use equation 5.3.6 to compute the model visibilities using the truncated sum obtained by the use of SVD. A set of basis functions with their corresponding coefficients is obtained by computing the SVD of $\mathbf{B}$ in Equation 5.3.6. We have Equation (5.3.11):

$$\mathbf{B^T} = \mathbf{U} \sum \mathbf{W^H} \tag{5.3.11}$$

Stellenbosch University https://scholar.sun.ac.za

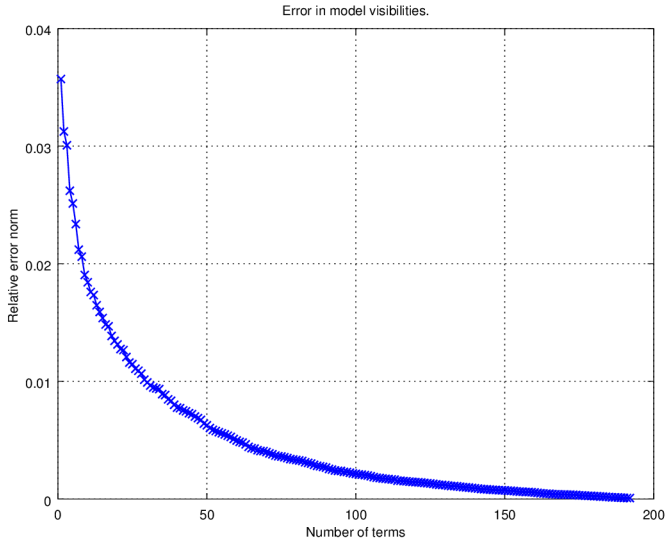

Figure 5.2: Accuracy of the forward calculation vs number of basis functions

The columns in the $N_p^2 \times N_B$ matrix U are basis functions and it follows that each expansion coefficient is an entry in the i^{th} row and k^{th} column as the basis. The model basis functions are achieved by interpolation of each singular vector in order to increase its support to a $N_p \times N_p$ grid, orthonomarlize the result to get $\{f_i\}_{i=1}^{N_B}$ and then every coefficient is computed by projecting the i^{th} basis to the k^{th} column of B^T.

The error between the measured visibilities $\mathbf{v}_{measured}$, which are the visibilities measured using equation 5.3.2 and the model visibilities $\mathbf{v}_{model}$ measured using equation 5.3.6 or equation 5.3.2 with is computed using the following equation.

$$\epsilon = \frac{||\mathbf{v}_{measured} - \mathbf{v}_{model}||^2}{||\mathbf{v}_{model}||^2} \tag{5.3.12}$$

Stellenbosch University https://scholar.sun.ac.za

5.4 A-Stacking: Backward calculation

The backward calculation is essentially the imaging process and is concerned with the conversion of equation 5.2.4. It has been discussed that this inversion is rarely performed directly and therefore nonlinear methods are used. In this section we discuss the adoption of the CLEAN algorithm by the A-Stacking framework without implementing it.

5.4.1 CLEAN adapted within the A-Stacking framework

The CLEAN algorithm has already been discussed in this work, therefore here we will demonstrate how CLEAN is adapted in the A-Stacking algorithm [3]. Consider a dirty image obtained by computing an inverse FT of the visibilities in equation 5.3.2.

$$\boldsymbol{\sigma_d} = \frac{1}{K}\boldsymbol{\Phi}^{\boldsymbol{H}}\mathbf{v} \tag{5.4.1}$$

Substituting equation 5.3.6 into 5.4.1, we obtain the following:

$$\boldsymbol{\sigma_d} = \frac{1}{K}\boldsymbol{\Phi}^{\boldsymbol{H}}\sum_{i=1}^{N_B}\text{diag}(\mathbf{a}_i)\boldsymbol{\Phi}\text{diag}(\mathbf{f}_i)\boldsymbol{\sigma} \tag{5.4.2}$$

Finally, the dirty image is given by equation 5.4.3, where the PSF is given by equation 5.4.4.

$$\boldsymbol{\sigma_d} = \sum_{i=1}^{N_B}\sum_{s=1}^{N_s}\sigma^s f_i(l_s,m_s)\mathbf{q}_i(s) \tag{5.4.3}$$

$$\boldsymbol{p_s} = \sum_{i=1}^{N_B} f_i(l_s,m_s)\left[\frac{1}{K}\boldsymbol{\Phi}^{\boldsymbol{H}}\text{diag}(\mathbf{a}_i)\boldsymbol{\Phi}\mathbf{e}_s\right] \tag{5.4.4}$$

here $\mathbf{e}_s$ is an image corresponding to a point source of unit intensity at location (l_s,m_s) on an empty sky, $\mathbf{q}_i$ is the PSF centered at (l_s,m_s). This dirty image is of the form of a sum of sub-images, different apparent skies that are convolved with an associated PSF $\mathbf{q}_i$. The CLEAN algorithm needs the PSFs $\{\boldsymbol{q}_i\}_{i=1}^{N_B}$ to be pre-computed, and $\boldsymbol{\sigma}_r$ be the residual dirty image at the start of the CLEANing. The procedure proceedes as follows:

1. The PSFs $\boldsymbol{q}_i$ are weighted by corresponding basis functions towards the direction of the source $f_i(l_s,m_s)$ and the accumulated result from N_B basis functions yield the total PSF $\boldsymbol{p}_s$.

2. The PSF $\boldsymbol{p}_s$ is scaled by the loop gain γ and identified source intensity,

$$\boldsymbol{p}_s \leftarrow \gamma\sigma_r^{(s)}\boldsymbol{p}_s \tag{5.4.5}$$

3. The PSF is subtracted and the residual map is updated,

$$\boldsymbol{\sigma}_r \leftarrow \sigma_r - \boldsymbol{p}_s \tag{5.4.6}$$

The above procedure elaborates the adaptation of CLEAN into the A-Stacking framework.

Stellenbosch University https://scholar.sun.ac.za

5.5 Conclusion

In this chapter we have discussed and implemented the A-Stacking framework, showing its performance in addressing the problem of DD-BD effects. This chapter made use of the ideas that were discussed in the preceeding chapters; we have seen that the complexity of the algorithm scales linearly with increasing number of basis functions. Therefore, a basis is efficiently computed using the Singular Value Decomposition (SVD). The SVD computes a basis which still generates the vector space **B** and only the nonzero singular values are taken. The DD-BD effects that were studied in this work are those caused by mutual coupling which were accounted for and simulations obtained using FEKO. In this chapter we have shown the simple trade-off between cost and acuuracy as offered by the algorithm.

Stellenbosch University https://scholar.sun.ac.za

Chapter 6

Results and Conclusions

6.1 Introduction

In this chapter we present the simulation results assessing the performance of the *Högbom* Clean algorithm and the A-Stacking algorithm. We demonstrate the perfomance of the *Högbom* Clean for both point sources and extended sources. This chapter integrates the whole thesis and discusses the results of the *Högbom* Clean implementation and the A-Stacking algorithm, illustrating the whole process from the simulated sky.

6.2 The Simulation Procedure

In order to implement the A-Stacking algorithm and *Högbom* Clean, we have to simulate the whole process of recovering the sky from the sampled visibilities. However, to have the sampled visibilities in the first place; we have to simulate antenna arrays both LOFAR-like and PAPER-like and account for the mutual coupling.

This is because the A-Stacking algorithm aims to correct for the DD-BD effects which are caused by a number of factors which we idealise for this work and only consider mutual coupling, but need to be kept in mind when considering the whole measurement process. Here we present the results starting from the antenna simulations, uv-coverages, dirty beams and dirty maps; the *Högbom* clean and the A-Stacking algorithm.

6.2.1 The Simulated Sky

Matlab code was used to simulate two sky models as shown earlier, one model consisting of point like sources and the other model consisting of extended sources. The sky images computed are 512×512 pixels each and the sources were random-

Stellenbosch University https://scholar.sun.ac.za

ized in a manner that they are located not less than 20 pixels from the edges. The brightness of the sources was varied randomly between $0-1$ mJy and the different cases were examined to test the capabilities of *Högbom* CLEAN. The figures below represent the matlab generated skies, both extended source in figure 6.1 and point sources in figure 6.2.

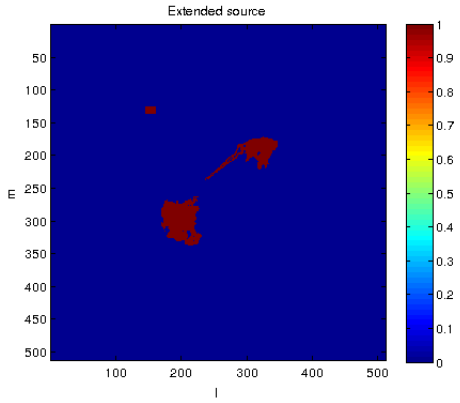

Figure 6.1: Sky model of the extended source simulated using Matlab.

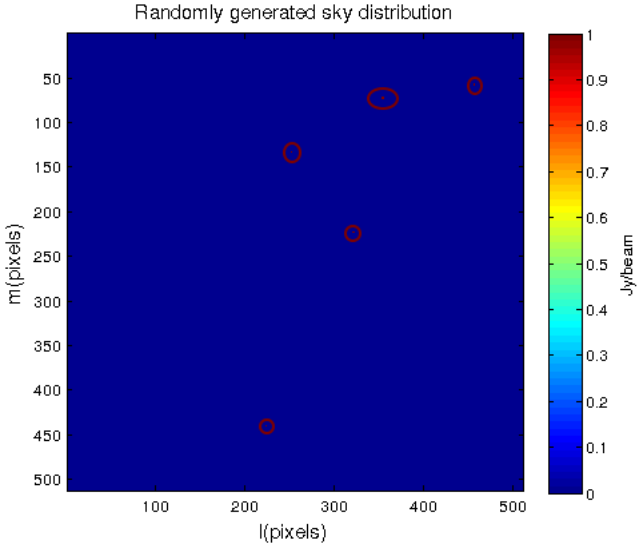

Figure 6.2: 5 random point sources of varying intensities simulated in Matlab.

6.2.2 The uv-Coverage

In order to be able to have the uv-coverage, two random array configurations for both the LOFAR-like and the PAPER-like arrays were simulated. These arrays were distributed randomly such that some of their baselines are short enough for

Stellenbosch University https://scholar.sun.ac.za

them to have mutual coupling, which is fully accounted for.

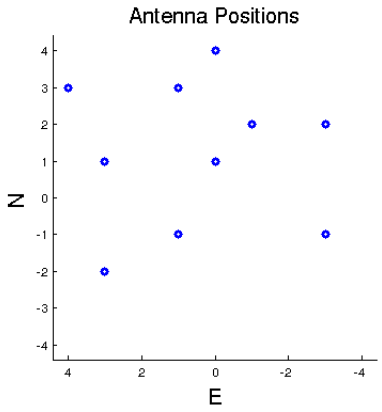

Figure 6.3: LOFAR LBA like random array

The configurations have been computed at 40° source declination and 35° observer latitude and 6 h hour angle. Varying the observation parameters like the declination, hour angle and even the antenna configuration itself affects the uv-coverage which ultimately affects the synthesized beam. Longer exposures increases the coverage and consequently idealises the synthesised beam as shown below.

These antenna configurations have been simulated to be coplanar (w = 0); the model of the sky and the corresponding visibilities were arranged into a uniform rectangular grid, such that each pixel in the intesity map corresponds to a pixel in the visibility map. The equivalent of this method is to multiply element-wise a sampling function (nail bed) to ungridded visibilities where the points of the visibility function are aligned to those of the sampling function.

6.2.3 The Dirty Map and Dirty Beam

The dirty map is the convolution of the dirty beam with the true sky; this means that the quality of the dirty map can be improved by fine tuning the dirty beam. In Chapter 2 the weighting functions used to fine tune the dirty beam are discussed. Here we show the effect of these functions below. In the Figures illustrate the effect of uv-coverage.

The Figure 6.4, illustrates the dirty beams corresponding to Figures 3.15 and 3.16. Each dirty beam is the corresponding result of taking the FT of each uv-coverage shown by uniform and natural weighting. From this figure, we note the different effects introduced by the different weighting functions to the PSFs.

Stellenbosch University https://scholar.sun.ac.za

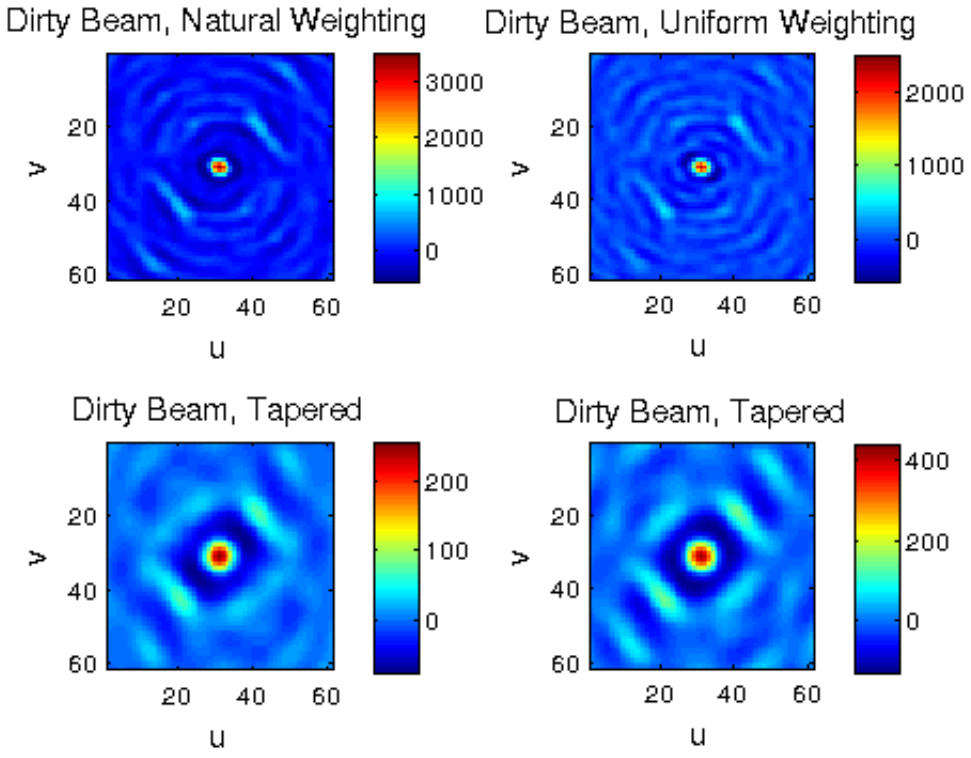

Figure 6.4: Weighted Beams

6.2.4 CLEAN results

The *Högbom* CLEAN algorithm has been implemented in Chapter 4 and shown to be performing better with point sources than extended sources. Here we show how the flux amplitude in the residual map decreases with increasing number of iterations. The original nature of the CLEAN algorithm is that it assumes sources to be resolved point sources and then iteratively subtracts them from the residual map until a noise-like structure remains at the bottom.

CLEAN then attempts to follow the same procedure for extended sources resulting in a poorer performance. The variants of CLEAN and other algorithms are better suited for extended sources, but fall outside the scope of this work and consequently were briefly mentioned. The figures below show the performance of CLEAN of extended structure and a graph showing residual flux amplitude decreasing with increasing iterations.

6.2.5 A-Stacking results

The A-Stacking algorithm was fully examined in Chapter 5 and has been shown to be an efficient alternative method for modeling DD-BD effects. The method

Stellenbosch University https://scholar.sun.ac.za

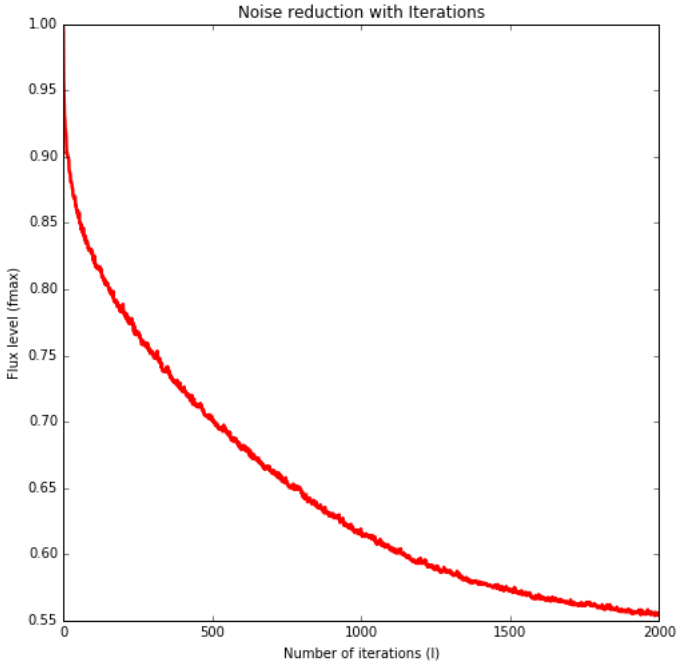

Figure 6.5: Flux amplitude decreasing with increasing number of iterations for an extended source structure.

provides a simple trade-off between computational efficiency and accuracy of the calculations; the trade-off is illustrated below as the error in forward calculation as a number of terms n_B.

6.3 Conclusion

This chapter summarizes and contexualizes the entire thesis. The simulation procedure has been discussed, starting from the antenna elements simulations by FEKO. A randomly distributed sky has been simulated, where all sources (point-sources) have been simulated to lie more than 20 pixels from the edges of the image. Visibilities were computed using this randomly generated sky together with an extended source random sky, computed using Matlab and dirty maps recovered. With the implementation of the *Högbom* Clean, plots showing the performance of Clean were shown. The *Högbom* Clean was shown to perform better with point-like sources as compared to extended structure. For extended structure, more iterations were needed as compared to the point-like sources to reduce the maximum flux levels.

The antenna arrays were simulated in such a way that the antennas lie in

Stellenbosch University https://scholar.sun.ac.za

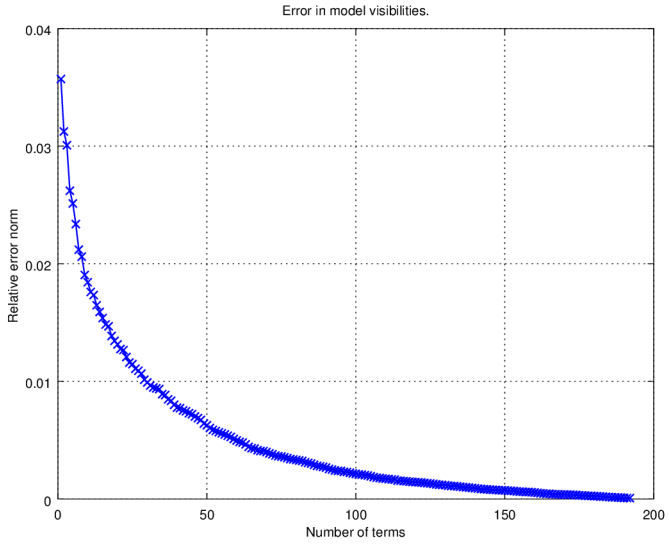

Figure 6.6: A simple tradeoff between the accuracy and the number of iterations (computational cost) of the A-Stacking algorithm.

close proximity to each other, so that they couple. Mutual coupling was fully incorporated in the simulations such that the A-Stacking algorithm was used to compute the forward calculation. The performance of A-Stacking shows that more terms yield better accuracy. The A-Stacking algorithm which caters for more general DD effects incorporates the Clean algorthm. One out of two ways of incorporating Clean is briefly mentioned in this work but not fully examined.

Stellenbosch University https://scholar.sun.ac.za

Chapter 7

Conclusion and Future Works

7.1 Conclusion

This chapter presents the concluding remarks and possible future works related to the work covered in this thesis. One would note that the main goal of this thesis was to implement the *Högbom* Clean and A-Stacking algorithms. However, the implementation of these algorithms are towards the far end of the chain of processes and simulations that are needed for that goal to be realised.

The physical characteristics of the PAPER and LOFAR arrays were used to simulate PAPER-like and LOFAR-like arrays. The simulated arrays are similar to PAPER and LOFAR in structure and operational frequencies, but in no way replicas of them. These simulations were shown in Chapter 2 to perform satisfactory for the purposes of this thesis. A 512×512 sky model was simulated in Matlab and the resulting synthesized map was CLEANed using the *Högbom* Clean algorithm. The *Högbom* Clean was shown to perform well for point sources than extended structure, which agrees with the expected results from literature. The loop gain was scaled to be 0.05 for both point source and extended structure, so that small scales were iteratively subtracted from the synthesized map. We note the Figures 4.10, 4.11, 4.6 and 4.5 that the number of iterations needed for the extended structure is much more than the point source, and yet the residual noise of the point source like structure is much lower than the extended source. This illustrates that the *Högbom* Clean performs better for point sources than extended structure.

Lastly and less trivial was the implementation of the A-Stacking algorithm. A 16×16 image grid was used and 5 randomly distributed sources of varying intensities were simulated. The forward calculation shows a simple trade-off, where the accuracy is inversely proportional to the number of terms used. From the first few terms, we note a rapid decrease in the relative error and as was expected, the error dissipates with increasing number of terms.

Stellenbosch University https://scholar.sun.ac.za

7.2 Future Works

The correction of DD effects is an active research field and the A-Stacking algorithm provides an alternative for solving more general BD-DD effects. The performance of the A-Stacking algorithm relies mostly on reducing the size of the convolution kernel. Further investigation in minimizing the size of the visibility convolution kernel and even possibly avoiding the convolution approach as it scales quadratically with increasing kernel size would be desirable [3].

Stellenbosch University https://scholar.sun.ac.za

Appendices

Stellenbosch University https://scholar.sun.ac.za

Appendix A

Radio Interferometry Measurement Equation

A.1 The Radio Interferometry Measurement Equation (RIME)

With the new generation of radio telescopes that are currently built by SKA, we want to make use of mathematically elegant formulations that will let us know what we can expect to observe with an interferometer, given a sky and the properties of the instruments [16]. The RIME is a mathematically elegant and complete description of what we actually measure with an interferometer [6]. Considering a sky consisting of a single source radiating electromagnetic waves in all directions, then at any position in space, a signal can then be described by a complex (2×1) vector $\mathbf{e}$ such that we have (A.1.1).

$$\mathbf{e} = \begin{pmatrix} e_x \\ e_y \end{pmatrix} \tag{A.1.1}$$

As this signal is propagating towards the interferometer, it is subjected to various transformations for which if all transformations are assumed to be linear, then each transformation can be represented by a (2×2) *Jones* matrix $\mathbf{J}$. The signal $\mathbf{e}'$ after the transformation can be related to the signal $\mathbf{e}$ before the transformation by a matrix multiplication $\mathbf{J}$.

$$\mathbf{e}' = \mathbf{J}\mathbf{e} \tag{A.1.2}$$

The $\mathbf{J}$ in the above equation is the total Jones matrix and since the signal undergoes multiple transformations as it propagates towards the interferometer, $\mathbf{J}$ can be expanded into its multiples corresponding to the physical transformations the

Stellenbosch University https://scholar.sun.ac.za

signal is undergoing [6]. The repeated matrix multiplication of **J** are known as the Jones chain and the order of occurence of the transformations must be maintained.

$$\mathbf{e}' = \mathbf{J}_n \mathbf{J}_{n-1} \dots \mathbf{J}_1 \mathbf{e} \tag{A.1.3}$$

Upon undergoing all these transformations, the signal continues propagating towards the interferometer until it impinges on the surfaces of the antennas and complex voltages are induced by the antenna feeds. Consider two antenna feeds, p and q then the voltage vectors V_p and V_q corresponding to the two feeds respectively are linear with respect to **e**.

$$\mathbf{V} = \begin{pmatrix} v_p \\ v_q \end{pmatrix} = \mathbf{J}\mathbf{e} \tag{A.1.4}$$

The above equation illustrates the linear relationship between the voltage vectors **V** as measured by the feeds of the antenna and the original signal vector **e** with **J** being the total Jones matrix. Considering two spatially separated antennas a and b that will measure independent voltages V_{pa} and V_{qb} respectively. The two independently measured voltages are correlated and give rise to 4 pairwise correlations between the components of V_a and V_b, such that when arranged will give the visibility matrix $\mathbf{V}_{pq}$ [57].

$$\mathbf{V}_{pq} = 2 \begin{pmatrix} \langle \mathbf{v}_{pa} \mathbf{v}_{qa}^* \rangle \langle \mathbf{v}_{pa} \mathbf{v}_{qb}^* \rangle \\ \langle \mathbf{v}_{pb} \mathbf{v}_{qa}^* \rangle \langle \mathbf{v}_{pb} \mathbf{v}_{qb}^* \rangle \end{pmatrix} \tag{A.1.5}$$

However, the visibility matrix can be written as the product of the column vector $\mathbf{v}_p$ with the transpose of the complex conjugate $\mathbf{v}_q^*$.

$$\mathbf{V}_{pq} = 2\langle \begin{pmatrix} v_{pa} \\ v_{qa} \end{pmatrix} \begin{pmatrix} v_{pb}^* v_{qb}^* \end{pmatrix} \rangle = 2\langle \mathbf{V}_p \mathbf{V}_q^H \rangle, \tag{A.1.6}$$

where $\mathbf{V}_q^H$ indicates the Hermitian transpose. From the arbitrary vector **e**, the signal to the different antennas a and b travels in different paths such that each propagation path has its own Jones matrices $\mathbf{J}_p$ and $\mathbf{J}_q$ respectively. Knowing that $\mathbf{V}_p = \mathbf{J}_p \mathbf{e}$ and $\mathbf{V}_q = \mathbf{J}_q \mathbf{e}$, then

$$\mathbf{V}_{pq} = 2\langle \mathbf{J}_p \mathbf{e} (\mathbf{J}_q \mathbf{e})^H \rangle = 2\langle \mathbf{J}_p (\mathbf{e}\mathbf{e}^H) \mathbf{J}_q^H \rangle. \tag{A.1.7}$$

Assuming that the Jones matrices are constant over the averaging interval, then

$$\begin{aligned} \mathbf{V}_{pq} &= 2\mathbf{J}_p \langle \mathbf{e}\mathbf{e}^H \rangle \mathbf{J}_q^H \\ &= 2\mathbf{J}_p \begin{pmatrix} \langle \mathbf{e}_x \mathbf{e}_x^* \rangle \langle \mathbf{e}_x \mathbf{e}_y^* \rangle \\ \langle \mathbf{e}_y \mathbf{e}_x^* \rangle \langle \mathbf{e}_y \mathbf{e}_y^* \rangle \end{pmatrix} \mathbf{J}_q^H \end{aligned} \tag{A.1.8}$$

Therefore we have the following:

$$2 \begin{pmatrix} \langle \mathbf{e}_x \mathbf{e}_x^* \rangle \langle \mathbf{e}_x \mathbf{e}_y^* \rangle \\ \langle \mathbf{e}_y \mathbf{e}_x^* \rangle \langle \mathbf{e}_y \mathbf{e}_y^* \rangle \end{pmatrix} = B. \tag{A.1.9}$$

Stellenbosch University https://scholar.sun.ac.za

The **B** denotes the brightness matrix. The first form of RIME is given by the following equation, which also ties the observed visibilities very elegantly with the intrinsic brightness **B** and the per-antenna Jones terms:

$$\mathbf{V}_{pq} = \mathbf{J}_p \mathbf{B} \mathbf{J}_q^H \tag{A.1.10}$$

Then by superposition principle, the interferometer response to a number of sources is the sum of the individual responses. Then finally for the case where the sky is not a sum of discrete sources but rather a continuous brightness distribution, the summation becomes integration over the portion of the sky say, S that is visible to the interferometer [6].

$$\mathbf{V}_{pq} = \int_s \mathbf{J}_p \mathbf{B} \mathbf{J}_q^H \tag{A.1.11}$$

The total Jones matrix **J** is the product of all the transformations that the signal has been subjected to. Thus, we can classify the Jones chain such that each matrice represents a particular transformation.

$$\mathbf{J}_p = \mathbf{G}_p \mathbf{E}_p \mathbf{K}_p \tag{A.1.12}$$

The Jones chain consists of various transformations, the transformations can be grouped to three groups. Transformations that occured before the electromagnetic waves were converted to electrical signal $\mathbf{K}_p$, these effects are towards the far right of the Jones terms and include effects such as phase delay, ionospheric effects and as well as parallactic rotation effects [16].

The transformations during the conversion of the EM waves to electrical signals at the terminals of the antenna are defined by the radiation pattern of the antenna and are known as the DDE's $\mathbf{E}_p$. Lastly the transformations that occur after the signal conversion $\mathbf{G}_p$,these effects are towards the far left of the Jones terms and includes all effects such as electronic gains and are known as DIE's. Therefore the focus of this work will be on DDE's, which are defined by the deformations in the radiation patterns.

Stellenbosch University https://scholar.sun.ac.za

List of References

[1] Kraus, J.D.: *Practical Antenna Handbook*. 2nd edn. McGraw Hill, 2001.

[2] Djuknic, G.M.: Near and far field. June 2016.
Available at: `https://en.wikipedia.org/wiki/Near_and_far_field`

[3] Young, A., Wijnholds, S., Carozzi, T., Maaskant, R., Ivashina, M. and Davidson, D.: Efficient correction for both direction-dependent and baseline-dependent effects in interferometric imaging : An a-stacking framework. *astronomy and astrophysics*, pp. 1–11, 2014.

[4] Wijnholds, S.: Lofar configuration considerations as a design exercise for ska lofar configuration considerations as a design exercise for ska. *SKA MEMO 143*, pp. 1–76, 2012.

[5] Parsons, A. and Backer, D.: The precision array for probing the epoch of reionization: Eight station results. *Astrophysics*, vol. 139, April 2009.

[6] Thompson, R., Moran, J. and Swenson, G.: *Interferometry and Synthesis in Radio Astronomy*. 2nd edn. Wiley-VCH, May 2001.

[7] Taylor, G., Carilli, C. and Perley, R.: Synthesis imaging in radio astronomy ii. *ASP Conference Series*, vol. 180, 1999.

[8] Nijboer, R., Pandey-Pommier, M. and de Bruyn, A.: Lofar imaging capabilities and system sensitivity. *LOFAR MEMO 113*, July 2009.

[9] Parsons, A.R., Liu, A., Aguirre, J.E., Ali, Z.S. and Bradley, R.F.: New limits on 21 cm epoch of reionization from paper-32 consistent with an x-ray heated intergalactic medium at z = 7.7. *Astrophysics*, vol. 788, p. 106, June 2014.

[10] Ali, Z.S., Parsons, A.R., Zheng, H., Pober, J.C., Liu, A., Aguirre, J.E., Bradley, R.F., Bernardi, G., Carilli, C.L., Cheng, C., DeBoer, D.R., Dexter, M.R., Grobbelaar, J., Horrell, J., Jacobs, D.C., Klima, P., MacMahon, D.H.E., Maree, M., Moore, D.F., Razavi, N., Stefan, I.I., Walbrugh, W.P. and Walker, A.: Paper-64 constraints on reionization: The 21 cm power spectrum at z = 8.4. *Astrophysics*, vol. 809, p. 61, August 2015.

[11] Offringa, A., Wayth, R., Kaplan, D., Barry, N. and Beardsley, A.: The low-frequency environment of the murchison widefield array : Radio-frequency interference analysis and mitigation. *Astrophysics*, vol. 32, 2015.

Stellenbosch University https://scholar.sun.ac.za

[12] Vos, M.D.: Lofar: The first of a new generation of radio telescopes. *ICASSP, IEEE Int. Conf. Acoust. Speech Signal Process. - Proc.*, pp. 865–868, 2005.

[13] Gugliucci, N. and Bradley, A.R.: Paper : The precision array to probe the epoch of reionization. *astronomy and astrophysics*, pp. 1–7, 2006.

[14] Backer, D. and Collaboration, P.: Recent results from the precision array for probing the epoch of reionization (paper) experiment in south africa. vol. 42 of *Bulletin of the American Astronomical Society*, p. 406. January 2010.

[15] Van Ardenne, A. and Bregman, J.: Extending the field of view with phased array techniques: Results of european ska research. *Proc. IEEE*, vol. 97, pp. 1531–1542, 2009.

[16] Young, A.: *Improving the Direction-Dependent Gain Calibration of Reflector Radio Telescopes*. PhD, Stellenbosch University, 2013.

[17] Bhatnagar, S., Rau, U. and Golap, K.: Wide-field wide-band interferometric imaging: the wb a-projection and hybrid algorithms. *Astrophysics*, pp. 1–10, 2013.

[18] Rau, U., Bhatnagar, S., Voronkov, M. and Cornwell, T.: Advances in calibration and imaging techniques in radio interferometry. *astro-ph.IM*, 2009.

[19] Bhatnagar, S., Cornwell, T., Golap, K. and Uson, J.: Correcting direction-dependent gains in the deconvolution of radio interferometric images. *Astronomy and Astrophysics.*, vol. 487, pp. 419–429, 2008.

[20] Hogbom, J.: Hogbom's clean algorithm. impact on astronomy and beyond. *Astronomy and Astrophysics*, 2009.

[21] Braun, R. and van Cappellen, W.: Aperture arrays for the ska: Dense or sparse? *SKA MEMO 87, ASTRON*, November 2006.

[22] Warnick, K.F., Maaskant, R., Ivashina, M.V., Davidson, D.B. and Jeffs, B.D.: High-sensitivity phased array receivers for radio astronomy. *IEEE*, vol. 104, March 2016.

[23] Lui, Hoi Shun ; Hui, H.T. and Bialkowski, M.: Mutual coupling in antenna arrays 2011. *Int. J. Antennas Propag.*, pp. 1–48, 2012.

[24] Wijnholds, S.: *Fish-Eye Observing with Phased Array Radio Telescopes*. PhD, Delft University of Technology, 2010.

[25] Briggs, D.: *High Fidelity Deconvolution of Moderately Resolved Sources*. Ph.D. thesis, The New Mexico Institute of Mining and Technology, Soccorro, New Mexico, March 1995.

[26] Balanis, C.: *Antenna Theory: Analysis and Design*. John Wiley and Sons, 2012.

[27] Carr, J.J.: *Practical Antenna Handbook*. 4th edn. McGraw Hill, 2001.

[28] Milligan, T.A.: *Modern Antenna Design*. 2nd edn. Wiley-IEEE Press, 2005.

Stellenbosch University https://scholar.sun.ac.za

[29] Young, A. and Davidson, D.: ' seeing ' radio waves. vol. 9, no. 2, pp. 24–30, 2013.

[30] Hui, H.T., Bialkowski, M.E. and Lui, H.S.: Mutual coupling in antenna arrays. *Int. J. Antennas Propag.*, pp. 2–4, 2010.

[31] Ellingson, S.: Sensitivity of antenna arrays for long-wavelength radio astronomy. *IEEE Trans. Antennas Propag.*, vol. 59, no. 6, pp. 1855–1863, 2011.

[32] Pozar, D.: Microstrip antenna aperture-coupled to a microstripline. *Electron. Lett.*, vol. 21, p. 49, 1985.

[33] Tasse, C., van Diepen, G. and et al: Lofar calibration and wide-field imaging. *Comptes Rendus Phys.*, vol. 13, pp. 28–32, 2012.

[34] Noorishad, P., Wijnholds, S.J., van Ardenne, a. and van der Hulst, J.M.: Redundancy calibration of phased-array stations. *Astron. Astrophys.*, vol. 545, 2012.

[35] Cheng, C., Jacobs, D. and et al: Paper-128 status update: Towards a 21cm power spectrum detection. *American Astronomical Society Meeting Abstracts*, vol. 227, January 2016.

[36] Pober, J., Parsons, A. and Aguirre, J.: Opening the 21 cm epoch of reionization window: Measurements of foreground isolation with paper. *Astrophysics*, vol. 768, p. 36, May 2013.

[37] Pober, J. and et al: Opening the 21 cm epoch of reionization window : Measurements of foreground isolation with paper. *Astronomy*, vol. 36, 2013.

[38] Parsons, A.: Interferometry ii. June 2015.
Available at: `Availableat:https://casper.berkeley.edu/astrobaki/index.php/Basic_Interferometry_II`

[39] Wilson, T.: Techniques of radio astronomy. *Astrophysics*, p. 47, 2011.

[40] Cornwell, T., Golap, K. and Bhatnagar, S.: The non-coplanar baselines effect in radio interferometry: The w-projection algorithm. *Astrophysics*, 2008.

[41] Rau, U., Bhatnagar, S., Voronkov, M. and Cornwell, T.: Advances in calibration and imaging techniques in radio interferometry. *Proc. IEEE*, vol. 97, pp. 1472–1481, 2009.

[42] Bhatnagar, S., Cornwell, T., Golap, K. and Uson, J.: Correcting direction-dependent gains in the deconvolution of radio interferometric images. *astron-ph*, 2008.

[43] Young, A., Maaskant, R., Ivashina, M., De Villiers, D. and Davidson, D.: Accurate beam prediction through characteristic basis function patterns for the meerkat/ska radio telescope antenna. *IEEE Trans. Antennas Propag.*, vol. 61, pp. 2466–2473, 2013.

[44] Bregman, J.D.: Some history behind the measurement equation calibration and self-calibration. *Astron-ph*, 2013.

Stellenbosch University https://scholar.sun.ac.za

[45] Goodrick, L.: *Image Reconstruction in Radio Astronomy with Non-Coplanar Synthesis Arrays*. Master's thesis, Stellenbosch University, Stellenbosch, South Africa, 2015.

[46] Hogbom, J.: Aperture synthesis with a non-regular distribution of interferometer baselines. *Astr. Astrophysics*, vol. 15, p. 417, June 1974.

[47] Jeffs, B.D., Tol, S.V.D. and Veen, A.-j.V.D.: Direction dependent self calibration of large distributed sensor arrays. *Astron ap*, pp. 1069–1072, 2006.

[48] Carozzi, T.: Simple estimation of all-sky, direction-dependent jones matrix of primary beams of radio interferometers. *Astron. Comput.*, 2014.

[49] Starck, J.-l. and Murtagh, F.: Deconvolution. *Handb. Astron. Data Anal.*, pp. 61–93, 2002.

[50] Offringa, A., Mckinley, B., Briggs, F. and et al: Wsclean : an implementation of a fast , generic wide-field imager for radio astronomy. *Astrophysics*, vol. 14, pp. 1–14, 2014.

[51] Tasse, C., van der Tol, S., van Zwieten, J., van Diepen, G. and Bhatnagar, S.: Applying full polarization a-projection to very wide field of view instruments: An imager for lofar. *Astron. Astrophys.*, vol. 553, p. 13, 2013.

[52] Clark, B.: An efficient implementation of the algorithm 'CLEAN'. *Astron. Astrophys.*, vol. 89, p. 377, 1980.

[53] Cornwell, T., Golap, K. and Bhatnagar, S.: The noncoplanar baselines effect in radio interferometry: The w-projection algorithm. *IEEE J. Sel. Top. Signal Process.*, vol. 2, pp. 647–657, 2008.

[54] msu.edu: Clean algorithm. Available at: archive.lib.msu.edu/crcmath/math/math/c/c368.htm, May 2016.

[55] Smirnov, O.M.: Revisiting the radio interferometer measurement equation. iii. addressing direction-dependent effects in 21 cm wsrt observations of 3c 147. *astronomy and astrophysics*, p. 11, 2011.

[56] Tesse, C., van der Tol, S., van Zwieten, J., van Diepen, G. and Bhatnagar, S.: Applying full polarization a-projection to very wide field of view instruments: An imager for lofar. *Astronomy and Astrophysics manuscript*, 2013.

[57] Smirnov, O.: Revisiting the radio interferometer measurement equation. I. A full-sky formalism. *Astronomy and Astrophysics*, 2011.